www.sciencemag.org/content/351/6279/1284/suppl/DC1

Supplementary Materials for

The geology of Pluto and Charon through the eyes of New Horizons

Jeffrey M. Moore,* William B. McKinnon, John R. Spencer, Alan D. Howard, Paul M. Schenk, Ross A. Beyer, Francis Nimmo, Kelsi N. Singer, Orkan M. Umurhan, Oliver L. White, S. Alan Stern, Kimberly Ennico, Cathy B. Olkin, Harold A. Weaver, Leslie A. Young, Richard P. Binzel, Marc W. Buie, Bonnie J. Buratti, Andrew F. Cheng, Dale P. Cruikshank, Will M. Grundy, Ivan R. Linscott, Harold J. Reitsema, Dennis C. Reuter, Mark R. Showalter, Veronica J. Bray, Carrie L. Chavez, Carly J. A. Howett, Tod R. Lauer, Carey M. Lisse, Alex Harrison Parker, S. B. Porter, Stuart J. Robbins, Kirby Runyon, Ted Stryk, Henry B. Throop, Constantine C. C. Tsang, Anne J. Verbiscer, Amanda M. Zangari, Andrew L. Chaikin, Don E. Wilhelms, New Horizons Science Team

*Corresponding author. E-mail: jeff.moore@nasa.gov

Published 18 March 2016, *Science* **351**, 1284 (2016)
DOI: 10.1126/science.aad7055

This PDF file includes:

Materials and Methods
Supplementary Text
Figs. S1 to S15
Table S1
References

Materials and Methods

Acronym List

AIM - al-Idrisi Montes
CM – Clarke Mons
CR - Cthulhu Regio
DEM – Digital Elevation Model
EH - encounter hemisphere
GRAIL - Gravity Recovery and Interior Laboratory
KBO - Kuiper Belt object
KM - Kubrick Mons
LEISA - Linear Etalon Imaging Spectral Array
LHB - Late Heavy Bombardment
LORRI - Long Range Reconnaissance Imager
MM - Mordor Macula
MVIC - Multispectral Visible Imaging Camera
PM – Piccard Mons
SFD - size-frequency distribution
SP - Sputnik Planum
TD - Tartarus Dorsa
TR - Tombaugh Regio
VP – Vulcan Planum
WM – Wright Mons

Derivation of stereo digital elevation models

All of the topography maps (or digital elevation models, DEMs) in this paper have been created using stereo photogrammetry. Our stereo method is an automated photogrammetry package based on scene-recognition algorithms, which attempt to match albedo patterns in finite-sized patches in each of two stereo images that observe a particular area on a planetary surface at different angles, from which parallax and the corresponding difference in elevation between points can be determined. This technique has been successfully applied to the Galilean and saturnian satellites (e.g. *24-29*), and we refer the reader to these references for detailed information on its construction and implementation. Stereo DEMs are reliable at regional scales, but are unable to resolve fine scale topographic features that are smaller than approximately five times the resolution of the poorest resolution image in the stereo pair due to pixel averaging. The technique is most effective for terrains that display pronounced albedo contrasts across a small spatial scale; low-contrast, featureless terrain will confuse the algorithm's attempt to match albedo patterns in the two stereo images. On Pluto, this becomes an issue when the technique is applied to low-contrast terrains including the high-albedo center of Sputnik Planum, and the low-albedo Cthulhu Regio, but outside these areas high quality DEMs are obtained.

We present data from three separate DEMs across six figures in this paper and the supplementary material: Figs. 2B, 3A, 5C, 6B, S6, and S14. Individual observations during the encounter are designated by name (e.g. P_MVIC_LORRI_CA):

- The DEM used in Figs. 2B, 3A, 5C and S6 was created using the MVIC P_MPan1 (495 m/pixel resolution) and MVIC P_MVIC_LORRI_CA (320 m/pixel resolution) observations as left and right images in the stereo pair. The resulting DEM can resolve features that are at least 2.5 km across, and has a vertical precision of 225 m.
- The DEM used in Fig. 6B was created using the MVIC C_MVIC_LORRI_CA (628 m/pixel resolution) and the LORRI C_MVIC_LORRI_CA (157 m/pixel resolution) observations as left and right images in the stereo pair. The resulting DEM can resolve features that are at least 3.1 km across, and has a vertical precision of 110 m.
- The DEM used in Fig. S14 was created using the MVIC C_Color_2 (1463 m/pixel resolution) and the LORRI C_LORRI (888 m/pixel resolution) observations as left and right images in the stereo pair. The resulting DEM can resolve features that are at least 7.3 km across, and has a vertical precision of 1250 m.

Supplementary Text

Sputnik Planum

The high albedo of the plains of Sputnik Planum (all names used on Pluto and Charon are informal) is consistent with a composition dominated by N_2 ice. N_2, CO, and CH_4 have all been detected within Sputnik Planum by the LEISA (Linear Etalon Imaging Spectral Array) spectral imager, although the relative amounts have not yet been modeled (*8*). Globally, however, N_2 is the dominant surface ice on Pluto (*30*), and we take nitrogen-dominated ice within Sputnik Planum as our working hypothesis.

The central and northern regions of Sputnik Planum display a distinct cellular morphology, which varies in appearance across the Planum. In the bright central portion of the Planum (Fig. S4A, corresponding to a region relatively high in CO ice as indicated by LEISA (*5*, *8*)), the cells are bounded by troughs that typically reach a few kilometers across and around a hundred meters deep, and which often display central ridges reaching ~1 km across. In some instances, dark material collects within these troughs. The cellular morphology is most apparent at the southern margin of this region (Fig. S4A). In the center of Sputnik Planum, the trough network becomes less interconnected. In the north of Sputnik Planum, where the cell interiors appear darker (Fig. S4B), cell boundaries are represented less by sharply-defined troughs and more by bright, diffuse lineations, which show no apparent relief, possibly due to infilling or relaxation. At the northernmost margin of Sputnik Planum (Fig. S4C), still darker ice is encountered, where it concentrates around the cell boundaries, which here appear thin (~1 km wide) and dark and show no apparent relief. Indications of flow in the form of swirl patterns and topographic embayment are apparent here (*5*), as well as near Hillary Montes (~5° N, 170° E) and between these Montes and Cthulhu Regio to the west (Fig. S1C).

Ice plains within the southernmost region of Sputnik Planum exist as two large lobes extending either side of Norgay Montes (~15° S, 175° E, Fig. S1C). The plains here, and on the eastern and western margins of Sputnik Planum, do not display cellular morphology, instead appearing featureless or showing dense concentrations of pits (Fig. S4D). Individual pits reach a few kilometers across, and show planforms ranging from equidimensional to elongate. Sublimation of the plains ice may form these pits, perhaps through a process similar to formation of the 'Swiss cheese features' in the south polar CO_2 ice cap of Mars (*31*); nitrogen ice on Pluto plays an analogous role to CO_2 ice on Mars, maintaining Pluto's atmosphere in vapor pressure equilibrium. Pits in Sputnik Planum are seldom seen within the cellular terrain relative to the southern and eastern plains, perhaps indicating that convection within the cellular terrain allows resurfacing of the ice on a timescale sufficient to eliminate any pits that form due to sublimation; the dense concentrations of pits within the southern and eastern plains would therefore imply that these plains are comparatively older than the cellular terrain.

These plains also feature streaks that appear to be composed of dense clusters of aligned pits with dark material covering their floors, and which seem to define the outlines of elongated cells, but which do not display any apparent relief (left-hand side of Fig. S4D). These 'ghost cells' are adjacent to the cellular terrain of Sputnik Planum, and the dark material may once have filled the troughs of actively convecting cells, which have since relaxed and lost their relief. Because of the noticeably stretched planforms of the pits and cell outlines in a ~N-S direction, the loss of relief may have been due to the nitrogen ice having flowed southward, thereby moving away from heat flow or other conditions that permitted convection within the cellular terrain of Sputnik Planum. Without convection to renew the surface and maintain cell relief, the dark material that once filled the troughs remains as the only indicator of the cells' existence, and its low albedo may cause heating of the nitrogen ice below, promoting sublimation and pit formation. The lack of a deeper heat source would, in contrast, help to maintain the relief of these pits by inhibiting their closure via inwards flow of bright, cold nitrogen ice.

In the eastern portion of Sputnik Planum where it borders the pitted uplands, numerous isolated hills that typically reach a few km across are scattered across the plains (Fig. S4E). They often form densely packed, generally elongate clusters that reach up to 20 km long, and, in the case of Challenger Colles (see Fig. S1B), form a rectangular, well-defined unit that measures 60 km by 35 km. Where these hills occur in the cellular terrain, they are almost exclusively coincident with the cell boundaries. Virtually no hills are seen in Sputnik Planum beyond ~250 km from the boundary with the pitted uplands. Close to the pitted uplands, groups of these hills tend to form chains that are coincident with the paths of glaciers emanating from the uplands. Isolated hills within smooth plains seen in the pitted uplands are hypothesized to be embedded fragments of the pitted uplands material (see main text section on this subject), and in Sputnik Planum the chains of hills may represent such fragments that have been carried out of the uplands by the putative glaciers into Sputnik Planum. If so, they may well have a water ice-based composition, allowing them to float on the nitrogen and/or carbon monoxide ice (which have very similar densities), as the chaotic mountains and smaller blocks on the western margin of Sputnik Planum are hypothesized to do (see next section). Once the fragments transfer from the glacial regime to the cellular regime, they would be subject to the solid-state convection motions of the nitrogen ice, and would move to the cell boundaries and congregate into densely packed groups. Challenger Colles may be an especially large accumulation of these fragments, perhaps where many of them have become grounded on a shallow substrate, one beneath the nitrogen ice-dominated layer.

Isostasy in Sputnik Planum

Water ice Ih has a solid density of 0.935 g/cm^3 in the temperature interval between 40 and 100 K (*32*). Water ice is elastic and brittle at those temperatures, so fractures and porosity created through geological processes (such as the prominent impact cratering on the west margin of SP or tectonics) can be maintained through geologic time as long as pressures and temperatures remain modest (*33*). We note for comparison that GRAIL (lunar mission) gravity data has conclusively shown that the lunar crust sustains porosities of 4–20% to considerable depths (at least several kilometers) (*34*), consistent with its bombardment history. Pluto's upper water ice crust, as exposed in its prominent mountains, could thus be underdense compared with solid ice, with densities between 0.90 and 0.75 g/cm^3 for a similar range of crustal porosities as on the Moon.

Solid N_2 densities vary between 1.00 g/cm^3 at 36 K (close to Pluto's present nitrogen ice surface temperature) and 0.942 g/cm^3 at the N_2 melting temperature at vapor pressure equilibrium of 63.15 K (*37*). Nitrogen ice is deformable enough at Pluto surface conditions (*6, 7*) that below any near-surface frost layer it will anneal into a coherent, crystalline solid. Hence whether solid or porous, water ice blocks will be buoyant in a layer of solid N_2.

For water ice blocks of 0.80 g/cm^3 (15% porosity) floating in isostatic equilibrium in "warm" but solid N_2 of 0.96 g/cm^3, emergent topography could be supported by ice keels of 0.8/(0.96 – 0.8) = 5 times vertical extent, if the topography were mirrored. Of course, the actual keel necessary for isostasy would depend on the specific keel topography, but this calculation suggests that ice mountains on Pluto up to a kilometer in height could easily float, or have floated, on a layer of solid N_2 a few km deep. Indeed, the mountains within Sputnik Planum rather resemble the angular blocks in europan chaos, i.e. fragments of pre-existing ice crust that have been detached by fracturing, transported, and rotated (*35*).

The origin of the basin in which Sputnik Planum is located is unknown, but it may be the site of an ancient impact basin (*36*), in which case a depth of a few km is quite plausible (for comparison, the observed depth of the largest confirmed impact crater on Charon is 6 km; see main text). On the other hand, the requirements for isostasy of the highest peaks found within Sputnik Planum (those in excess of 3-km height) are more severe (keels possibly in excess of 15 km), and likely exceed any plausible depth for the volatile ices that make up Sputnik Planum. There is, however, the possibility that relatively dense volatile ices accumulating within a broad impact basin could lead to isostatic adjustment of Pluto's crust as a whole, in the manner of accumulating sediments in the Gulf of Mexico and sedimentary basins elsewhere on Earth. In this case the total thickness of Sputnik Planum's volatile ices could be much larger than estimated from pristine basin depths on other icy bodies (*26*). An important caveat, which might limit deep N_2 ice layers, is that in the absence of solid state convection (discussed below), N_2 ice should melt at depths of a couple of kilometers or so for present-day heat flows (*38*), and liquid N_2 is relatively buoyant (0.8 g/cm^3).

Other volatile ices in Sputnik Planum

As noted above, CO and CH_4 ice have also been identified within Sputnik Planum. Spectroscopy alone cannot, however, determine the bulk composition of SP's volatile ices at kilometers depth. Nitrogen is the most volatile of these ices, is the major constituent of Pluto's sublimation-supported atmosphere (>99% (*12*)), and therefore must be the principal material component in Pluto's glacial cycle. Arguments developed in this paper for the buoyancy of water-ice-rich blocks and the piedmont-glacier-style flow of volatile ice onto the surface of SP (Fig. 3A), as opposed to the latter's sinking into the Planum as a density current, imply that the Planum is not dominated by low-density CH_4-rich ice (density ≈ 0.5 g/cm^3). Hence in discussing SP we focus on N_2-dominated ices, while recognizing that CO-rich ice may be important at depth in the SP volatile-ice layer. CO and N_2 share the same molecular weight, and have numerous solid-state properties in common (*39*). As crystalline solids they form a nearly complete solid solution with each other (*40*) and the density of CO ice is only about 1.5% greater than that of N_2 ice over the temperature range of interest (*39*). So in terms of buoyancy or bulk thermal properties, we can treat N_2 and CO as the same.

Solid-state Convection

The cellular pattern observed over much of Sputnik Planum is suggestive of convective upwellings and downwellings (*5*), and we show here that the rheology of weak, van der Waals bonded ices such as N_2 (or CO) likely permits solid-state overturn within a multi-km thick layer on Pluto.

N_2 ice in laboratory experiments exhibits uniaxial strain rates at 56 K (0.89 T_m, where T_m is melting temperature) of 2×10^{-4} s^{-1} at differential stresses of 100 kPa (1 bar) (*7*), equivalent to a viscosity $\eta \sim 2 \times 10^8$ Pa-s. This is orders of magnitude less viscous than water ice near its melting temperature at similar stresses (~10^{13} Pa-s for temperate glacier ice (*41*)). The viscosity of N_2 ice is also temperature dependent. For the activation energy Q^* assumed for volume diffusion of 8.6 kJ/mole (*6*), the natural exponential viscosity temperature scale $\delta T = RT^2_{ad}/Q^*$, where R = the gas constant and T_{ad} is the adiabatic temperature of the potentially convecting layer, is only 3 K if T_{ad} = 56 K (see, e.g., *42-44*). The temperature difference across the layer, ΔT, which would drive the convection, is limited by the long-term average surface ice temperature (perhaps 36 K (*45*)) at the top and the N_2-ice melting temperature (63 K) at the bottom, or ≈ 27 K. This maximum ΔT in turn implies a maximum (linearized) viscosity ratio ($\Delta\eta$) from top to bottom of $\exp(\Delta T/\delta T) \sim 10^4$.

Activation energies were not derived in (*7*), but their data indicate a smaller Q^* (see next section) and thus a larger δT (~6K) and smaller $\Delta\eta$ than suggested above. In either case, the viscosity ratio across a layer of solid nitrogen will be limited and not be high enough to place it into the stagnant lid convective regime (*43, 44*). Most importantly, for a range of Rayleigh numbers *Ra* (the dimensionless measure of the vigor of convection) above the critical value for the onset of convection, Ra_{cr}, convection proceeds in the so-called sluggish or mobile lid regime. In this regime, the surface is in motion and transports heat, but moves at a much slower pace than the deeper, warmer interior. As such it is characterized by large aspect ratio convective cells (e.g., *46*), which would be consistent with observed cell dimensions of 20-30 km if the Sputnik Planum layer thickness were at least several kilometers.

The rheologies measured by (*7*) are mildly non-Newtonian (stress dependent with power law indices n ~2), and as such it is important to consider convective stress levels (σ). These are given by $\sigma \sim 10^{-1} \times \alpha\rho g h \delta T$, where α is the volume thermal expansion coefficient (2×10^{-3} K^{-1} for N_2 ice (*37*)), g is surface gravity (0.617 m/s^2), and h is the vertical scale associated with δT, often the convective boundary layer thickness, i.e., a length scale smaller than the entire layer depth (*47*). Table S1 shows estimates of σ for some plausible combinations of h and δT, and from these, η values are derived from the flow laws measured for N_2 ice at either 56 K or 45 K (*7*). Such viscosity values in turn allow estimates of basal Ra_b, using these η and, for concreteness, a layer depth H of 4 km (note that Ra_b increases as H^3). The Ra_b values in Table S1 are all well above the Ra_{cr} for sluggish lid convection (*44*). Moreover, an empirical scaling for sluggish lid convection (*48*) can be used to estimate the surface heat flow $Nu \times k\Delta T/H$, where Nu is the Nusselt number, the dimensionless measure of heat flow, and k is the thermal conductivity (0.2 W/m·K for N_2 ice (*37*)). For example, assuming $Ra_b = 10^6$ and $\Delta\eta = 10^3$, scaling gives $Nu \sim 4.5$, which translates to a heat flow of ~ 4.5 mW/m^2 for a total ΔT of 20 K over 4 km. This is close to the expected radiogenic heat flow from Pluto today, several mW/m^2 (*14*, *49, 50*).

Comparing this latter value with the heat flow estimates in Table S1, we see some estimates exceed Pluto's likely present-day heat flow. This can be interpreted in two ways. One is that the T_b assumed in a given case in Table S1 is too high. But another is that solid state convection in N_2 ice occurs readily, and may occur in layers much thinner than 4 km, and thus would be likely capable of transporting even higher heat flows, such as those in the distant geologic past.

The values of Ra_b and $\Delta\eta$ in Table S1 are not meant to precisely define the convective parameters for Sputnik Planum. Rheological understanding of N_2 ice is simply too limited. For example, volume diffusion has been previously argued on theoretical grounds to be the dominant creep mechanism in N_2 ice (e.g., *38*), although unless the ice grain sizes are very small, it is more likely that the relatively soft, power-law creep actually measured by (*7*) will be the dominant mechanism. In addition, CO ice readily forms a solid solution with N_2 ice. A sufficient concentration of CO would imply an orientationally ordered, α crystalline phase at Pluto temperatures, as opposed to the disordered, β-phase characteristic of N_2 ice at the same temperatures (*39*). The rheological properties of α-phase CO ice have not been measured to our knowledge, but based on the rheologies of ordered and disordered water ice phases (*51*), we anticipate that it is more viscous than β-N_2 ice at the same conditions.

Thus, the examples in Table S1 are simply meant to illustrate the plausibility of convective heat transport today within a sufficiently thick layer of relatively deformable, volatile ice. A more rigorous evaluation of convective modes on Pluto must also explicitly take into account the non-Newtonian character of N_2 ice creep. The same division into isoviscous, sluggish lid, and stagnant lid convective regimes occurs for non-Newtonian rheologies (*52*).

Glacial Flow of Nitrogen Ice

Owing to its weak crystalline bonding (noted above), N_2-dominated ices are expected to flow relatively quickly on the surface of Pluto. Much of the high relief topography observed on Pluto's surface is not expected to be supported by such material (*6*). In the following we examine the relaxation and flow timescales of N_2 ice based on available laboratory data.

As noted above, the steady-state creep of N_2 is non-Newtonian. The measured stress (σ) and strain-rate ($\dot{\epsilon}$) obey the power-law relationship (*7*):

$$\dot{\epsilon} = A(T)\sigma^{n(T)}, \qquad \text{(S1)}$$

with a temperature dependent pre-factor A and exponent n. The tangential, shear stress τ due to surface relief on Pluto is a function of the overlying mass and angle of the sloping surface. Assuming the pre-factor is an Arrhenius type of function of the form:

$$A(T) = A_{45}\exp\left(\frac{T_A}{45\text{ K}} - \frac{T_A}{T}\right) \qquad \text{(S2)}$$

where $A_{45} = 0.005\ s^{-1}(\text{MPa})^{-n(T)}$, fitting the data reported in Table 1 of (*7*) shows that the corresponding approximate value of the activation temperature is T_A = 422 K (equivalent to a Q^* = 3.5 kJ/mole). The value of the exponent n, which hovers around 2.1 in the temperature range of interest, suggests that the underlying creep mechanism may be grain boundary sliding (e.g. *53*). A simple linear fit of the same data set gives $n(T) = 2.1 + 0.0155\,(T/\mathrm{K} - 45)$.

The inverse of the strain rate, $\dot{\epsilon}^{-1}$, gives a measure of the deformation timescale of ice structures. Assuming an ice layer of thickness H that is set at an angle θ with respect to the horizontal, the shear stress of the ice at the base of its layer is $\tau = \rho g H \sin\theta$. Taking the density of N_2 ice to be 986.5 kg/m^3 (its value at T=45K (*37*)), we can estimate the strain or deformation rate for N_2 ice structures by combining Eq. (1.1) with τ given together with the fitted form given in Eq. (1.2) to find:

$$\dot{\epsilon} \approx 442\mathrm{yr}^{-1} \cdot \left(\frac{H}{100\mathrm{m}}\right)^n \cdot (sin\theta)^n \cdot \exp\left[\frac{T_A}{45\ \mathrm{K}} - \frac{T_A}{T} - 0.091\mathrm{K}^{-1}(T - 45\ \mathrm{K})\right] \qquad \text{(S3)}$$

Thin ice layers with low sloping angles may be treated as a "shallow" flow since the magnitude of horizontal velocities u dominates vertical velocities w under such conditions (*54, 55*). Further, assuming a 1D flow with uniform interior temperature means one may write $\dot{\epsilon} = du/dz$ and vertically integrate Equation (S1) once to get an estimate for the horizontal flow speeds on the surface, which is given by $u_H \approx \dot{\epsilon} H/(n+1)$.

The above forms for both $\dot{\epsilon}$ and u_H allows us to make certain estimates. For example, we consider the time it takes a sloping channel with a given uniform depth of ice to completely drain itself out assuming this process takes place in the absence of basal melt. For N_2 ice at T=45 K and at a depth of 100 meters, together with a sloping angle of $\theta = 10°$, yields a unit strain time of $\dot{\epsilon}^{-1} \approx 1/11.5\ \mathrm{yr}$, or slightly longer than an Earth month. The surface of such an ice mass flows at an approximate rate of $u_H = 375$ m/yr, suggesting that the drainage time of a 10 km long channel at this grade is about 26 yr. By contrast, an ice layer with these dimensions but with a lower temperature T=38 K instead relaxes on a time scale of $\dot{\epsilon}^{-1} \approx 0.21\ \mathrm{yr}$, with a surface flow speed of

$u_H = 154$ m/yr. A similar ice layer, but with a much shallower slope angle θ = 0.5°, gives corresponding deformation timescales and flow rates of 84 yr and 0.39 m/yr respectively, whereupon a 100 km long basin is traversed by the surface flow in about 250,000 yrs. Inferred rates are very sensitive to the flow thickness assumed – it goes as roughly H^3 in this case.

The timescales quoted above are likely upper limits because the strongly insulating nature of N_2 ice will imply warmer interior temperatures. Temperature gradients through pure N_2 ice could be 20-25 K/km, given estimates of Pluto's current geothermal heat flux of ~4 mW/m^2 (*14, 49, 50*). The time it takes to achieve such a state can be estimated by the time it takes a simple thermal wave to traverse up a layer of thickness H with thermal diffusivity $\kappa = K / \rho C_p$. This gives an estimate for the e-folding thermal timescale of $t_{\mathrm{th}} = (H / 2\pi)^2 / \kappa$. For a heat capacity $C_p \approx 1500$ J/kg·K (*37*), the thermal equilibration time for plutonian N_2 ice is $t_{\mathrm{th}} \approx (H / 12\ \mathrm{m})^2$ yr.

This underscores the importance of assessing the timescales on which N_2 is deposited on the surface. If the surface deposition occurs at a rate of 0.5-2 cm/yr (*8*), then according to the above, ice layers grown at this rate will always be in thermal equilibrium given the emergent interior geothermal heat flux. A given vertically thick ice layer grown in this way will move faster than if the same layer had been placed in-situ all at once because the larger interior temperatures at the base in the slowly grown ice layer scenario imply much lower basal viscosities and, hence, higher flow rates.

Formation of Washboard Terrain

The regular, parallel patterning of the washboard terrain (Fig. 4A), with inter-ridge spacing of about 1 km and ridge lengths often of tens of kilometers, is difficult to explain. Sublimation can produce regularly-spaced landforms like penitentes and snow cups, but they tend to be nearly equidimensional (*56-60*). The large scale of the washboard texture is also problematic when compared to the meter to decimeter scale of terrestrial ablation topography. However, in many geomorphic systems large features can dominate and cannibalize initially smaller features if sufficient time and space exists. The lateral continuity of washboard ridges suggests if sublimation were the dominant process, the washboard crests would have had to migrate over long distances. Such long-distance migration through sublimation has produced the parallel troughs in the martian polar caps (*61*, *62*). We see no evidence, however, for systematic lateral migration in the case of the washboard terrain. If the sublimation process were influenced by persistent atmospheric circulation, lateral continuity could be related to wave-like structures and the interaction of sublimation and wind. The rarified modern atmosphere of Pluto, however, is unlikely to host such structures, but a denser prior atmosphere might also permit ice particle transport and transverse dune formation (*3*).

Alternately, the washboard terrain could potentially be related to the former presence of an ice cover over the landscape. An unusual type of low relief ground moraine topography has formed beneath some ice sheets on Earth called washboard or corrugated moraine (e.g., *63*), which is characterized by parallel ridge and swale topography (albeit with a shorter wavelength of 30-200 m). Its mode of origin is uncertain, but (*63*) suggest it forms beneath surging glaciers, due to formation of crevasses and injection of sediment from below. The origin of the consistent NE-SW orientation of ridges in Pluto's washboard terrain is also uncertain, but could be related to solar illumination, atmospheric circulation patterns, or glacial flow directions.

Formation of Dissected Terrain

As described in the main text, we identify five categories of dissected terrains on Pluto, examples of which are shown in Fig. 4B. Already discussed in the main text are fluted terrain, characterized by incision of downslope-oriented grooves at ~3 km spacing (red arrows), and dendritic valley networks (green arrows), which have branching linear depressions with deeper incision along the trunk valleys, somewhat analogous to terrestrial fluvial drainage basins. The three remaining varieties include dissected plateaus, which also have dendritic structure, but are characterized by modestly incised valleys on upland plateaus with a palmate structure emptying into deeply-incised trunk valleys; alpine valley systems, which are characterized by wide, dendritic trunk valleys (yellow arrow) that are straight to gently curving and which head on dissected mountainous slopes (orange arrow), that have a style of dissection similar to that of the fluted terrain; and mountainous dissection, which is characterized by steep, branched valley networks giving the appearance of dissected terrestrial mountain chains.

A variety of processes form valley-like morphology on Earth and the other planets. We consider below the major categories of such processes and evaluate whether they are possible contributors to one or more of the types of dissected terrains on Pluto.

1. Shear failure of the underlying materials. This could occur either through slow flow, as in terrestrial earthflows, which occasionally form dendritic complexes (*64*), or through failure due to rapid avalanching, such as occurs on terrestrial mountain slopes (*65*) and spur-and-gully terrain on the walls of the martian Valles Marineris. Triggering of such flows generally requires a critical slope gradient. Plutoquakes could also provide critical stresses.

2. Accumulation and avalanching failure of ices accumulated from the atmosphere. Snow avalanches contribute to chute erosion on terrestrial mountain slopes (*66*), and avalanching of seasonal CO_2 snows is one suggested mechanism for formation of martian gullies (e.g., *67*).
3. Surface ice accumulation, glacial flow, and erosion. This is the dominant mechanism for erosion by valley glaciers on Earth (e.g., *68, 69*).
4. Erosion beneath thick ice sheets, such as ice streams at the margins of terrestrial plateau glaciers, such as at Greenland and Antarctica (e.g., *70*).
5. Erosion by precipitation of volatiles such as rain or snow, followed by erosion by liquid runoff, which accounts for most terrestrial valley networks (e.g., *71*).

Mechanisms 1 and 2 could potentially contribute to formation of the steep fluted terrain, but are unlikely to contribute to erosion of the larger dendritic valleys. In addition, these mechanisms tend to deposit transported material close to their sources as fans or lobate deposits. Although image resolution may limit recognition, such depositional forms have not been identified. Terrestrial valley glaciers are competent agents of erosion, long-distance transport, and deposition. Most terrestrial valley glaciers occupy former fluvially-sculpted valley networks (e.g., *72*); whether ice accumulating on undissected uplands would sculpt dendritic valley networks is uncertain. Most terrestrial valley glaciers are warm-based, with meltwater production that contributes to basal sliding and accompanying substrate erosion by abrasion and quarrying (e.g., *73, 74*). Cold-based ice sheets on Earth and Mars have generally been considered to be inefficient in eroding their beds (*75, 76*). Recent studies, however, suggest that cold glacier beds can be eroded at modest rates by plucking and bed shear (*77, 78*). Erosion by nitrogen ice flowing over a water ice substrate on Pluto might be aided by the lower density of the latter. Thick enough accumulations of nitrogen-rich ices on Pluto (see Glacial Flow of Nitrogen Ice section) can result in basal melting under reasonable thermal gradients, which can lubricate the base of the glacier and substantially increase its capacity for erosion. Stereo imaging in the dendritic valley network and mountainous terrains suggests some valleys end in depressions or have irregular profiles, which is a characteristic of terrestrial valley glacier erosion (although post-formation processes may have affected the Pluto valleys). The valley networks of the plateau-dissected terrain on Pluto are suggestive of some terrestrial glacial valley networks with broad, deeply incised trunk valleys and hanging tributaries.

Erosion by precipitation and runoff is impossible in Pluto's current environment, and would require a dramatically thicker past atmosphere. Thus we conclude that the most reasonable explanation for formation of Pluto's dissected terrains is glacial erosion by former accumulations of nitrogen-rich ices.

Upland terrains: Fretted and eroded mantle terrain

Fretted terrain: Northwest of Burney crater (Fig. S1), fretted terrain consists of bright plains separated into polygons by a network of darker troughs 3 to 4 km wide (Fig. S5). Numerous craters (<25 km diameter) occur within this terrain, some with dark floors. The fretted terrain perhaps originated as tectonically disrupted blocks, whose margins were subsequently widened by glaciation and/or sublimation.

Eroded mantle terrain: An eroded mantle (i.e. material draping underlying topography) characterizes the high northern latitudes to the NE of SP (Fig. S3). The density of craters is low except for a few degraded examples ~50 km across. The mantle appears smooth with convex rounded edges (Fig. S6), and may be depositional. Locally the surfaces have been eroded by steep-sided pitting that reaches 3-4 km deep. The mantle has a relatively bluish tint (Fig. 1A) and is in excess of 1 km thick in places.

Western low latitude terrains

Smooth Plains: An extensive, low-elevation, mottled plain occurs at the western end of Innana Fossa (Fig. S1), bounded by an arcuate scarp along its southern and western borders (Fig. S7). It has a much lower crater density than surrounding regions. Despite the younger fracture system, it is significantly smoother than intercrater plains in adjacent areas. Scarp retreat appears to have been active in this region (see arrows highlighting Piri Rupes in Fig. S7).

Bright-halo craters: In Vega Terra, centered at 25°N, 125°E (Fig. S1), craters feature dark floors, bright rims and bright outer rim flanks, in contrast to craters elsewhere. Even within this subset of craters, there is variation in their colors and albedos (independent of sun angle), including between north- and south-facing slopes within the same crater (Fig. S8).

Tectonics

Fig. S9 displays several examples of prominent tectonic features across the encounter hemisphere of Pluto. Faulting that appears to have experienced little degradation is concentrated to the west of Sputnik Planum. These include the subparallel normal faults of Djanggawul Fossae, which emanate from Oort crater (Fig. S9E) and extend northwards for several hundred km (Fig. S9A). The segmented grabens of Inanna and Dumuzi Fossae are ~600 km long, reach 20 km wide and 2-3 km deep, and no rift flank uplift is observed for them (Fig. S9B). In Cthulhu Regio, the normal fault scarp of Virgil Fossa is ~950 km long and reaches 3-4 km high, and cuts Elliot crater at its eastern end (Fig. S9C). Beatrice Fossae, to the south of Virgil Fossa, reaches at least 450 km long, and a poorly illuminated south-trending set of fractures is located between Beatrice Fossae and Virgil Fossa, which trend at ~45° to the larger features. A heavily degraded graben system passes across the north pole; the graben shown in Fig. S9D reaches more than 100 km long. Fewer obvious manifestations of extensional faulting are seen to the east of Sputnik Planum, but ~550 km long Sleipnir Fossa is a prominent example, and in its southern portion is bounded on both sides by swells of Tartarus Dorsa (Fig. S9F). At the northern extent of Sleipnir Fossa, it becomes one of a set of fractures radiating from a central focus, which is similar in appearance to novae on Venus (*79*). The cause of the spatial orientation of Pluto's extensional features may be due to shell heterogeneities or other global stress-inducing mechanisms.

On Charon, Argo Chasma was viewed very obliquely along the horizon (*5*). In lower resolution images, it is seen to have an arcuate planform (Fig. S10), and so could be related to an impact basin, or alternatively, could be a continuation of the fracture/trough system that bisects Charon's encounter hemisphere.

Impact Craters

Crater albedo patterns and morphologies vary widely across Pluto (Figs. S11 and S12). Albedo patterns include many different combinations of bright or dark floors, rim walls, floor material, and/or central peaks. Craters at northern latitudes and to the north and east of Sputnik Planum display less albedo variation and are generally bright, but may be degraded or infilled. Crater degradation is apparent in a number of forms, including tectonic disruption, infilling of various kinds, and possible sublimation and mass wasting features (Fig. S12). Some of the bright floor material in various craters appears to be a smooth infilled deposit similar in color and appearance to Sputnik Planum, implying it may be a remnant of a once more extensive deposit, or has locally accumulated in topographic lows. Much of the dark infilling material also appears smooth. Dark infilling is likely tholin deposits (*8*).

Pluto crater statistics

The total cumulative crater distribution on Pluto's encounter hemisphere is shown in Fig. S13A. Because of variable lighting and Pluto's active geology, this distribution does not represent a production function (one representative of the impactor size-frequency distribution). It can, however, set a lower limit on ages. As in (*5*), model ages can be assigned according to estimates of the impacting Kuiper belt object (KBO) population (*11*). The KBO population is estimated at large (diameter $D \gtrsim 100$ km) sizes from astronomical observations and can be extrapolated to the smaller impactor sizes that make the observable craters under a variety of plausible assumptions; numerical integrations then provide estimates of the time rate of decay of the various Kuiper belt subpopulations. In (*11*), four models were presented for the overall size-frequency of Pluto's crater-forming impactor population, which cover a broad range of possible crater densities on Pluto's surface for any specific, true terrain age. Any measured crater density on Pluto can then be compared with these values, and different "model ages" determined. Characteristics of the measured crater size-frequency distribution may make a given model age more or less plausible.

On Pluto's encounter hemisphere, the cumulative density for $D \geq 20$ km is ~$3.5\mathrm{x}10^{-5}$ km^{-2}. Comparison with model predictions (Figs. 5 and 9 in (*11*)) yields ages 4 Ga or greater for all but one impact flux model. The single, younger model age (~500 million years) requires a very steep crater production function between 10- and 100-km crater diameter (i.e., many smaller impactors). Although the encounter hemisphere size-frequency distribution does steepen somewhat in this diameter range (cf. Fig. 12B), it is far from steep enough, so this model age is provisionally rejected (but see discussion of Charon crater statistics, next).

Crater densities for different Pluto terrains are shown in the relative differential, or R-plot, form (*80*), in Fig. S13B, with age predictions for the "broken power-law" KBO distribution from (*11*). The latter is probably the simplest, agreed-upon representation of the Kuiper belt population (*22*). Highly cratered regions are ancient for this flux model, whereas more lightly cratered regions indicate a wide range of crater retention ages on Pluto.

Charon crater statistics

Lighting precludes accurate crater counting in Charon's higher latitudes. Nevertheless, this region does contain several craters >50-km in diameter (*D*), consistent with great age (*81, 10*). In particular, for a cumulative crater density of (1.1 ± 0.3) x 10^{-5} km^{-2} for $D \geq 50$ km (13 such craters on ¼ of Charon's surface, Fig. S15A), all of the model ages in (*11*, cf. *82*, *83*), which account for the range of plausible impactor size-frequency distributions in the Kuiper belt, are nominally older than 4 billion years.

The relative smoothness of the southern plains (Vulcan Planum), and the low sun angles of the images, allow accurate crater counts down to ~4-km diameter. The plains may appear more cratered than the northern terrain, but this is an artifact of lighting and viewing geometry. The cumulative crater size-frequency distribution lies below that of the north at large diameters (Fig. S15A), indicating a relatively younger age. In particular the differential slope for Vulcan Planum craters > 10-km-diameter is –2.9 ± 0.3 and the downturn to a very shallow crater size-frequency distribution at diameters $\lesssim$ 10 km appears to be real. Cumulative crater densities down to 10-km diameter agree with those reported in (*5*) from early, lossy images, considering statistical uncertainty. When comparing measured crater densities for Charon (Figs. S15A and B) with predictions as shown in the size-frequency distributions of Fig. 12 in (*11*), both as cumulative and R-plot versions (and when corrected by a factor of 4 (*82*, *83*)), all model ages for the plains but one are 4 Ga or greater. As with Pluto, we discount the young model age, but much more firmly, and conclude that Vulcan Planum as a whole likely dates back billions of years.

Of all the terrains on Pluto or Charon on which to count craters, the southern plains of Charon offer the best representation of the flux of smaller KBOs over time. The illumination and viewing geometry are ideal for discriminating crater forms, and the plains themselves appear to offer a resurfaced "clean slate" upon which to identify craters. There are no obvious gross regional (e.g., east-west) variations in the impact crater density either. When viewed as an R-plot, the overall crater size-frequency distribution for Vulcan Planum appears "flat" in the ~10-to-100–km diameter range (Fig. S15B), and is inconsistent with those proposed KBO size distributions that are "steep" (possessing a relatively great abundance of smaller impactors) in this size range. Specifically, steep implies a power law index $q \gtrsim 4$, with q defined by the differential distribution $dN/dD \propto D^{-q}$. Moreover, the size-frequency distribution at smaller sizes ($\lesssim$10-km diameter) is exceptionally shallow. There is a distinct paucity of smaller craters, corresponding to a relative dearth of km-scale KBOs.

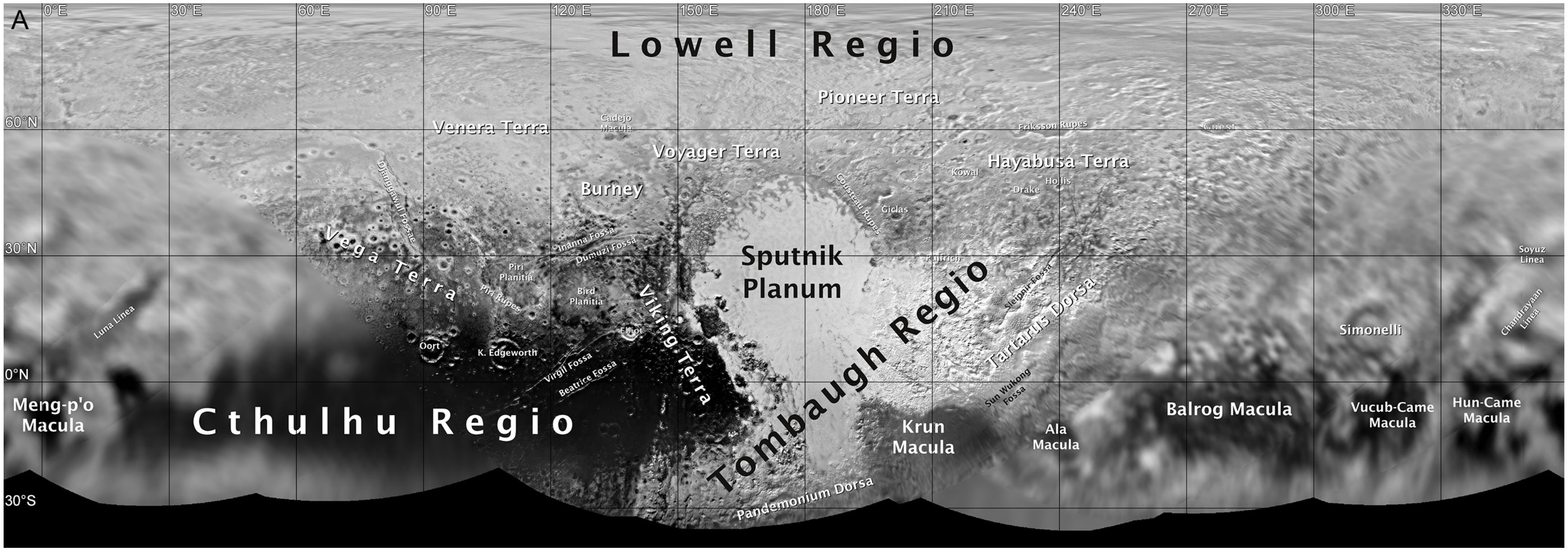
A
0°E
30°E
60°E
90°E
120°E
150°E
180°E
210°E
240°E
270°E
300°E
330°E
60°N
30°N
0°N
30°S
Lowell Regio
Pioneer Terra
Venera Terra
Cadejo Macula
Voyager Terra
Eriksson Rupes
Guest
Hayabusa Terra
Kowal
Hollis
Drake
Burney
Djanggawul Fossae
Cousteau Rupes
Giclas
Vega Terra
Inanna Fossa
Dumuzi Fossa
Sputnik Planum
Pulfrich
Soyuz Linea
Piri Planitia
Piri Rupes
Bird Planitia
Viking Terra
Tombaugh Regio
Sleipnir Fossa
Tartarus Dorsa
Chandrayaan Linea
Luna Linea
Elliot
Simonelli
Oort
K. Edgeworth
Virgil Fossa
Beatrice Fossa
Sun Wukong Fossa
Meng-p'o Macula
Cthulhu Regio
Krun Macula
Ala Macula
Balrog Macula
Vucub-Came Macula
Hun-Came Macula
Pandemonium Dorsa

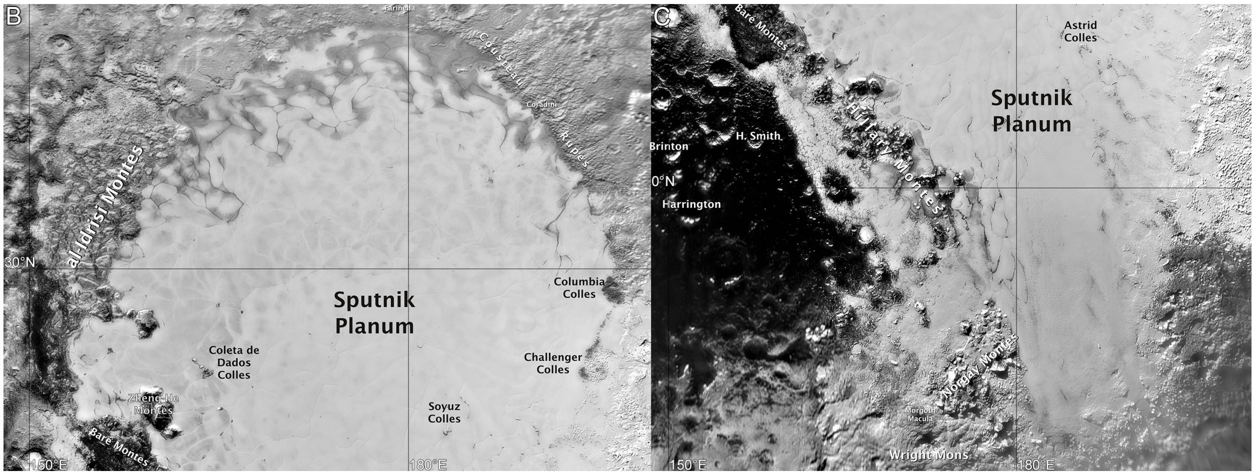

Fig. S1: **Informal nomenclature maps for Pluto.** These maps have been updated from those in (*5*) to reflect the names in this paper.

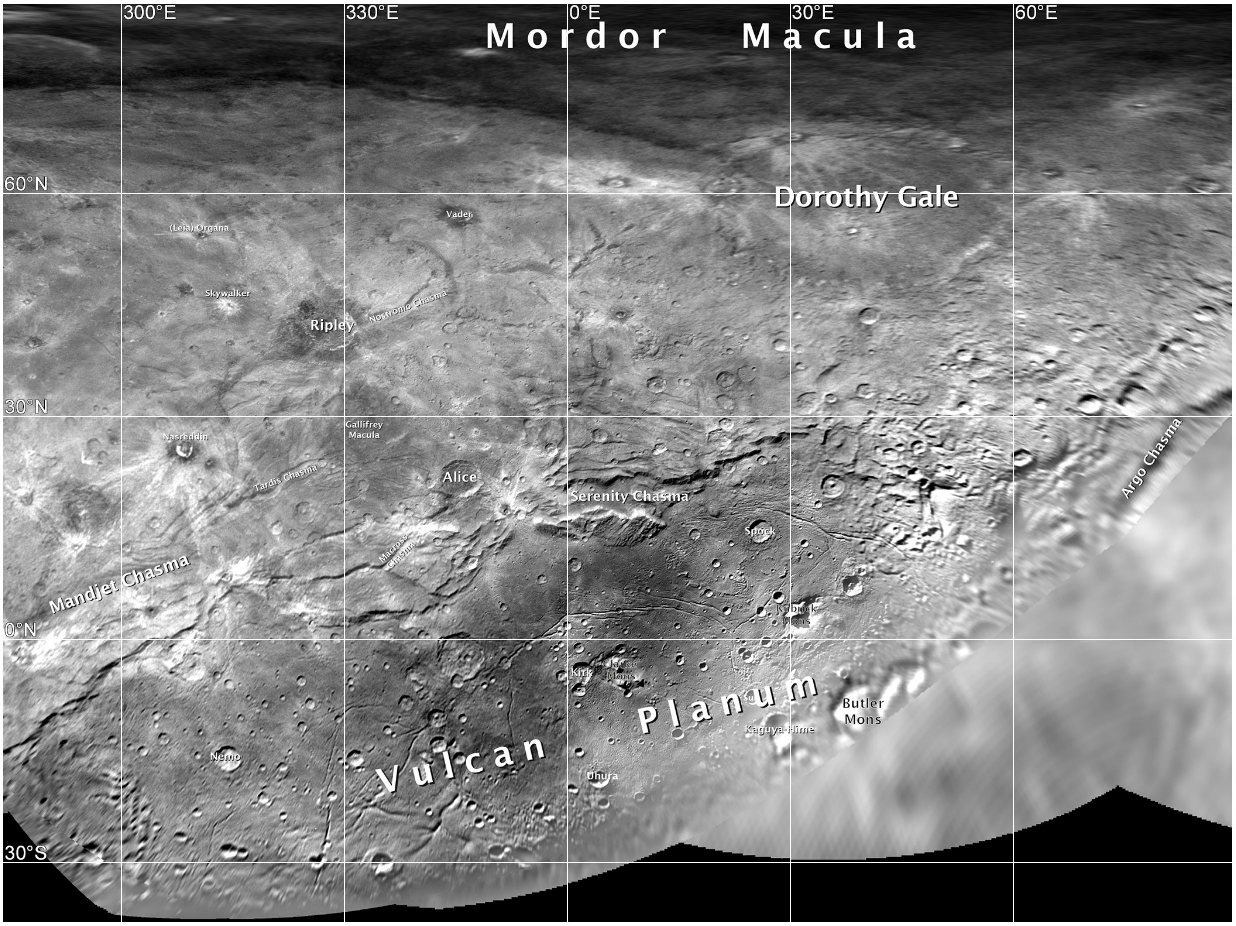

Fig. S2: **Informal nomenclature map for Charon.** This map has been updated from that in (*5*) to reflect the names in this paper.

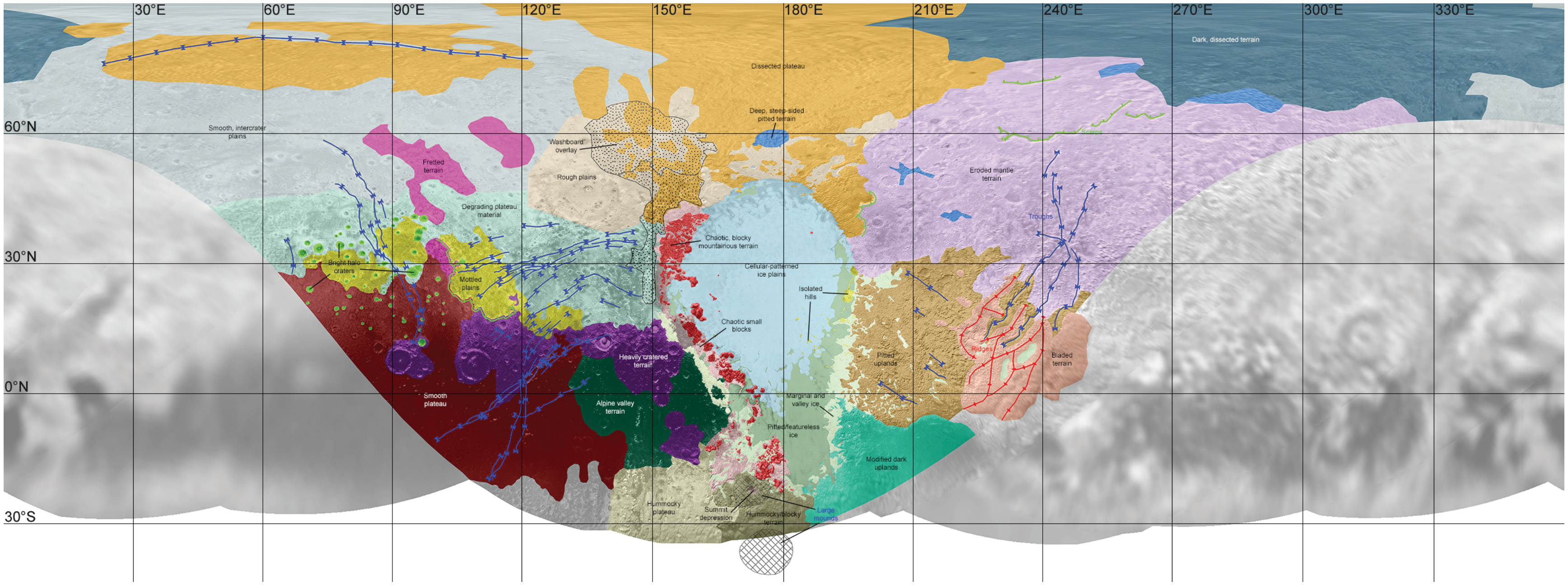

Fig. S3: **Simple cylindrical global projection of a terrain locator map for Pluto.** 180° longitude is located at the center of the figure. This figure should NOT be interpreted as a geological map in any way; rather it provides a general indication of where terrains that are described in the text are located on Pluto. Terrains within low-resolution zones are not mapped.

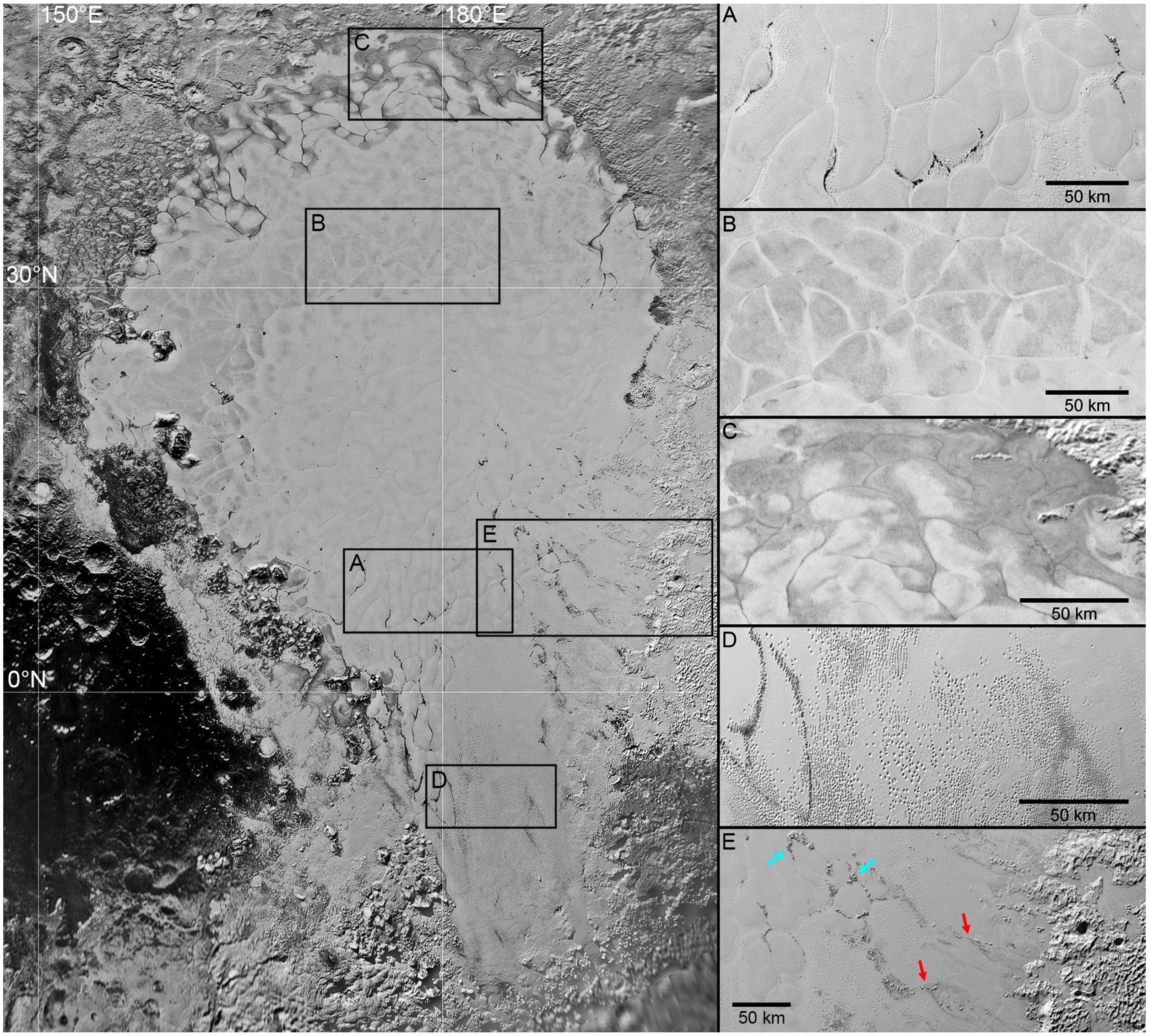

Fig. S4: **Reprojected LORRI mosaic of Sputnik Planum.** Details (at right) focus on different terrain types within the plains. Enhanced, detailed images are taken from 320 m/pixel, reprojected MVIC coverage of the P_MVIC_LORRI_CA observation. North is up in all instances. (a) Bright cellular terrain. (b) Dark cellular terrain. (c) Dark terrain displaying lobate flow patterns at the margin with the surrounding terrain. (d) Featureless and pitted plains. (e) Isolated hills in eastern Sputnik Planum, close to the boundary with the pitted uplands (seen on the right-hand side of the figure). Red arrows highlight chains of hills that are coincident with the paths of glaciers; blue arrows highlight coagulations of hills within the cellular terrain.

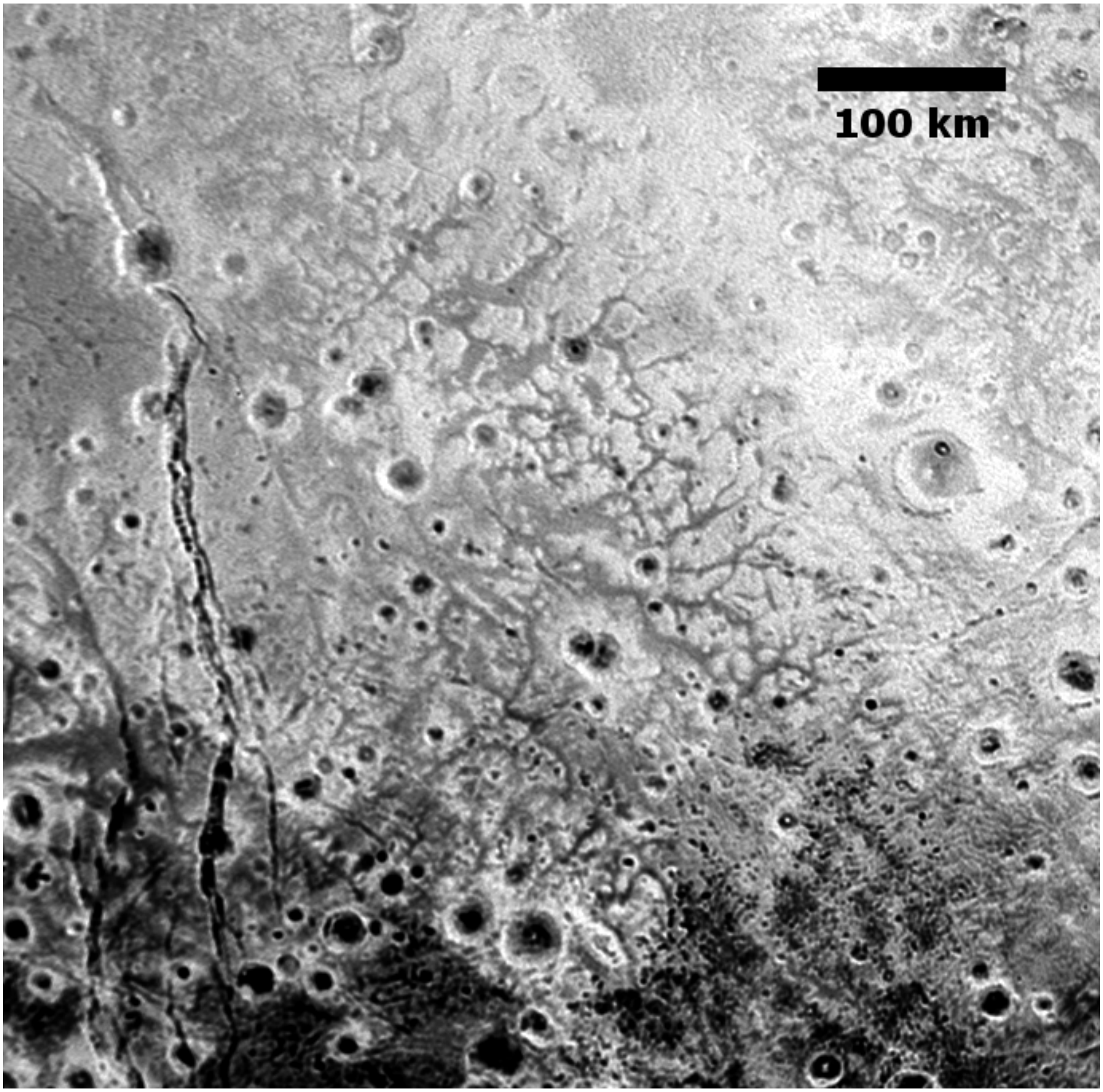

Fig. S5: **Fretted terrain located northwest of Sputnik Planum.** 890 m/pixel reprojected LORRI coverage from the P_LORRI observation, centered at 50.6°N, 97.2°E. North is up.

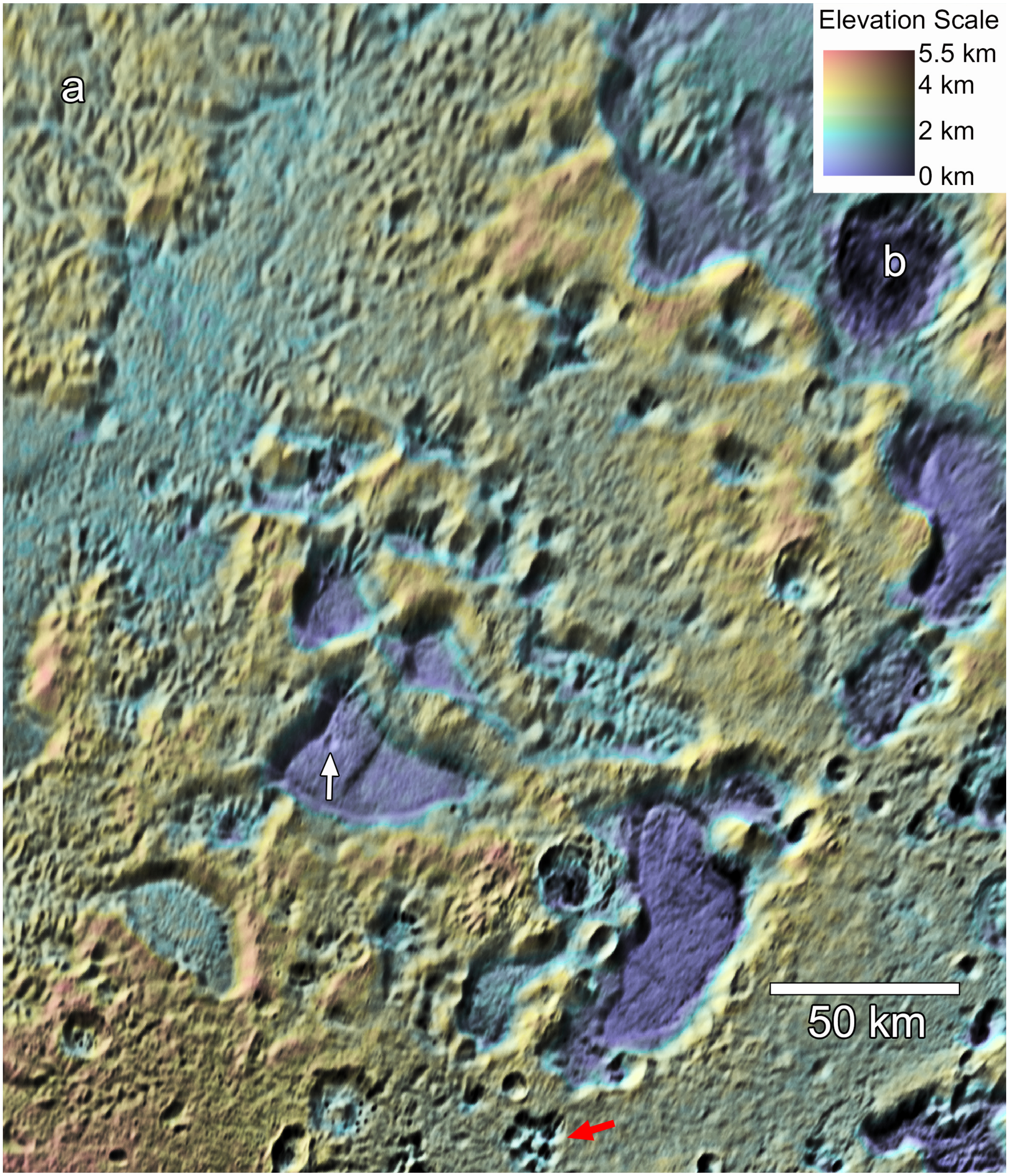

Fig. S6: **Deep, nearly flat-floored depressions in the eroded mantle terrain located northeast of Sputnik Planum.** Colorized DEM with 320 m/pixel, reprojected MVIC coverage from the P_MVIC_LORRI_CA observation overlain, centered at 59.9°N, 206.6°E. North is up. The depressions indent 1.8 to 3.5 km below the surrounding uplands. Given the numerous impact craters on the uplands and only one small crater on the depression floors (white arrow), it is unlikely that the uplands were deposited around pre-existing depressions. Local removal of upland deposits through selective sublimation is one possibility, as are resurfacing and associated erosion by cryovolcanic flows or accumulation of ices from condensation within pre-existing depressions. The depression floors reach up to ~3 km in depth below their rims. Smaller, pit-like depressions also occur at scattered locations (red arrow). A 33 km diameter crater is located at "b" and a region of dendritic valleys occurs at "a".

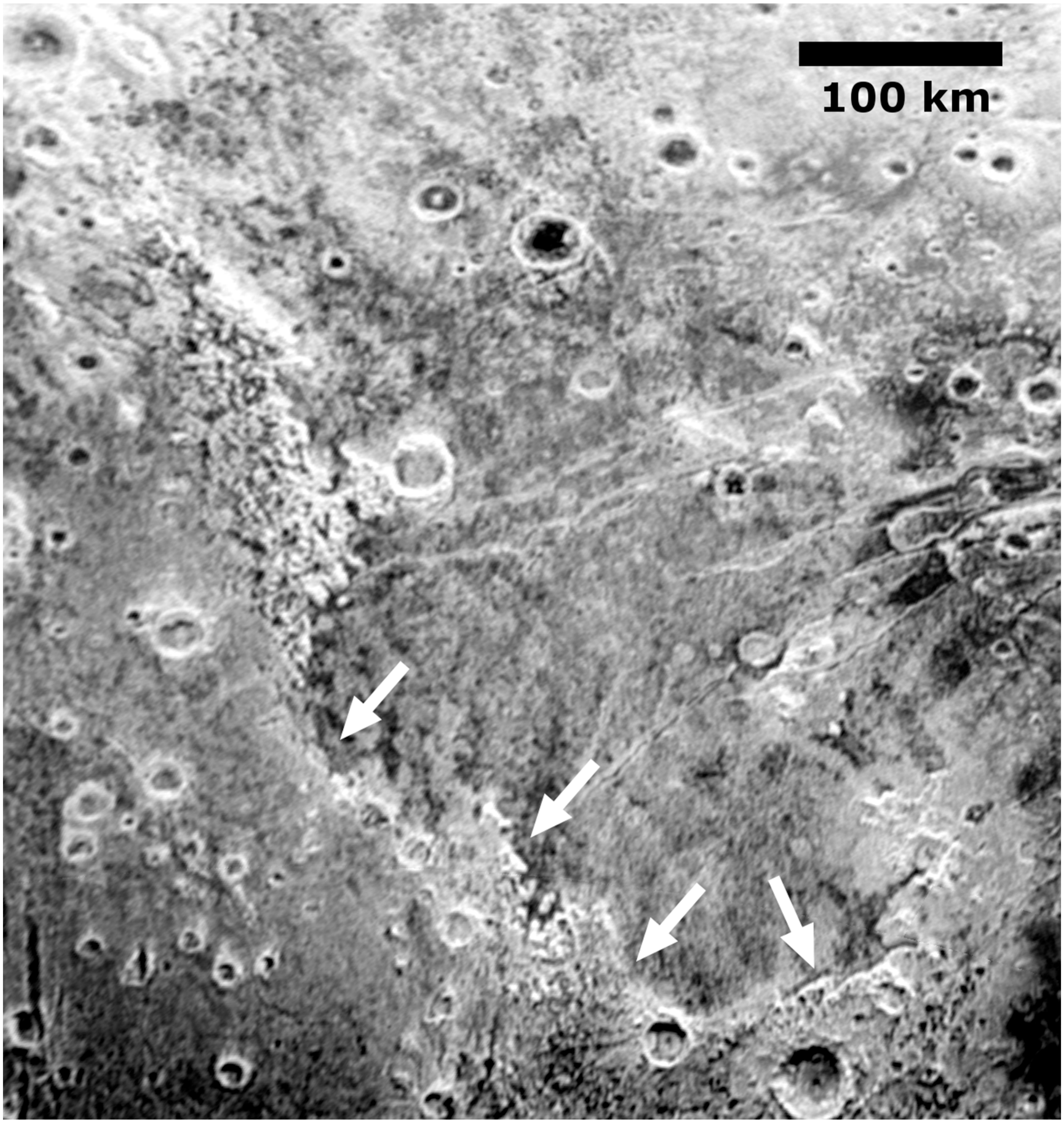

Fig. S7: **Mottled plains and a scarp located north of Cthulhu Regio.** 890 m/pixel, reprojected LORRI coverage from the P_LORRI observation, centered at 29°N, 109°E. North is up. The mottled plains in the center of the figure may have been exhumed by a scarp that surrounds them to the west and south (white arrows) that has undergone retreat. We cannot rule out the possibility that these plains may have also experienced subsequent resurfacing. Fractures from Innana Fossae cross these plains from the east.

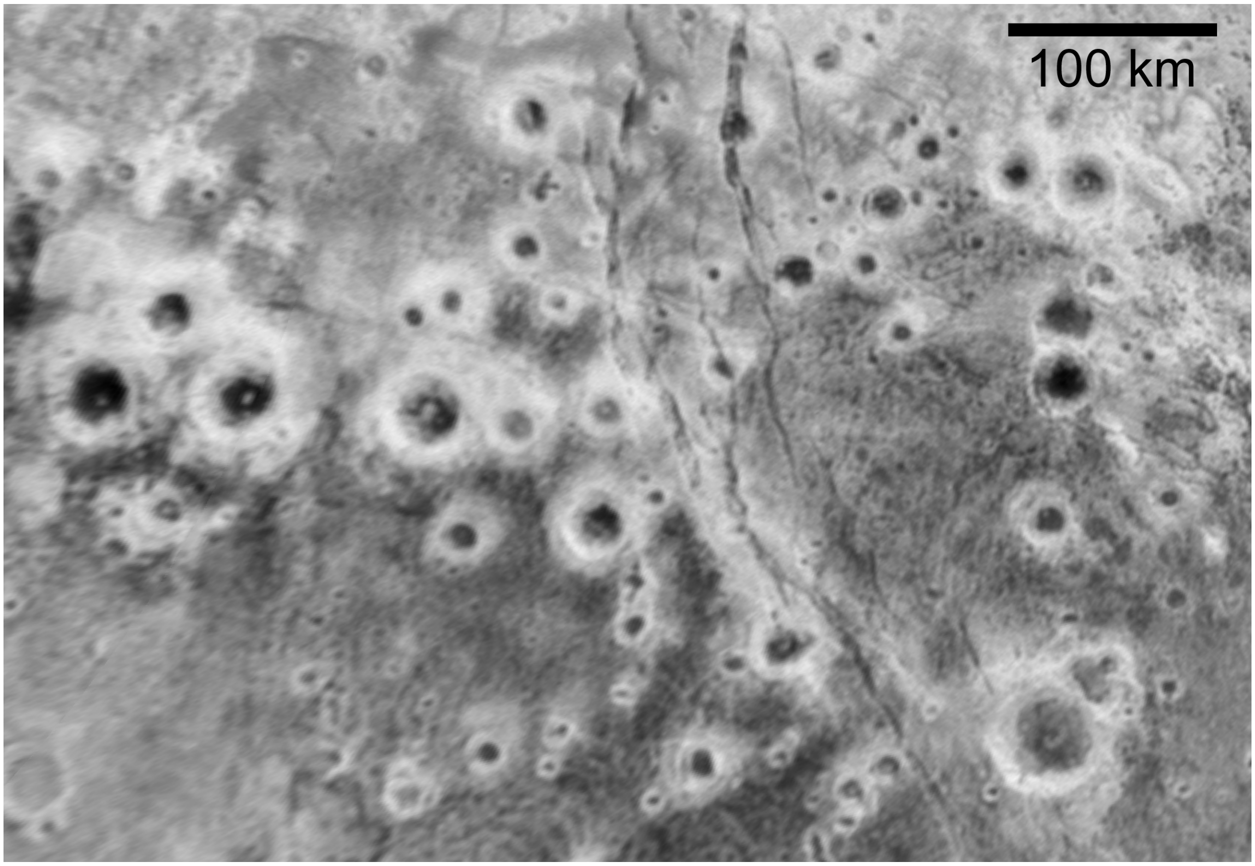

Fig. S8: **Bright-halo craters located in Vega Terra.** Djanggawul Fossae runs N-S through the center of the image. 890 m/pixel, reprojected LORRI coverage from the P_LORRI observation, centered at 34.3°N, 83.2°E. North is up.

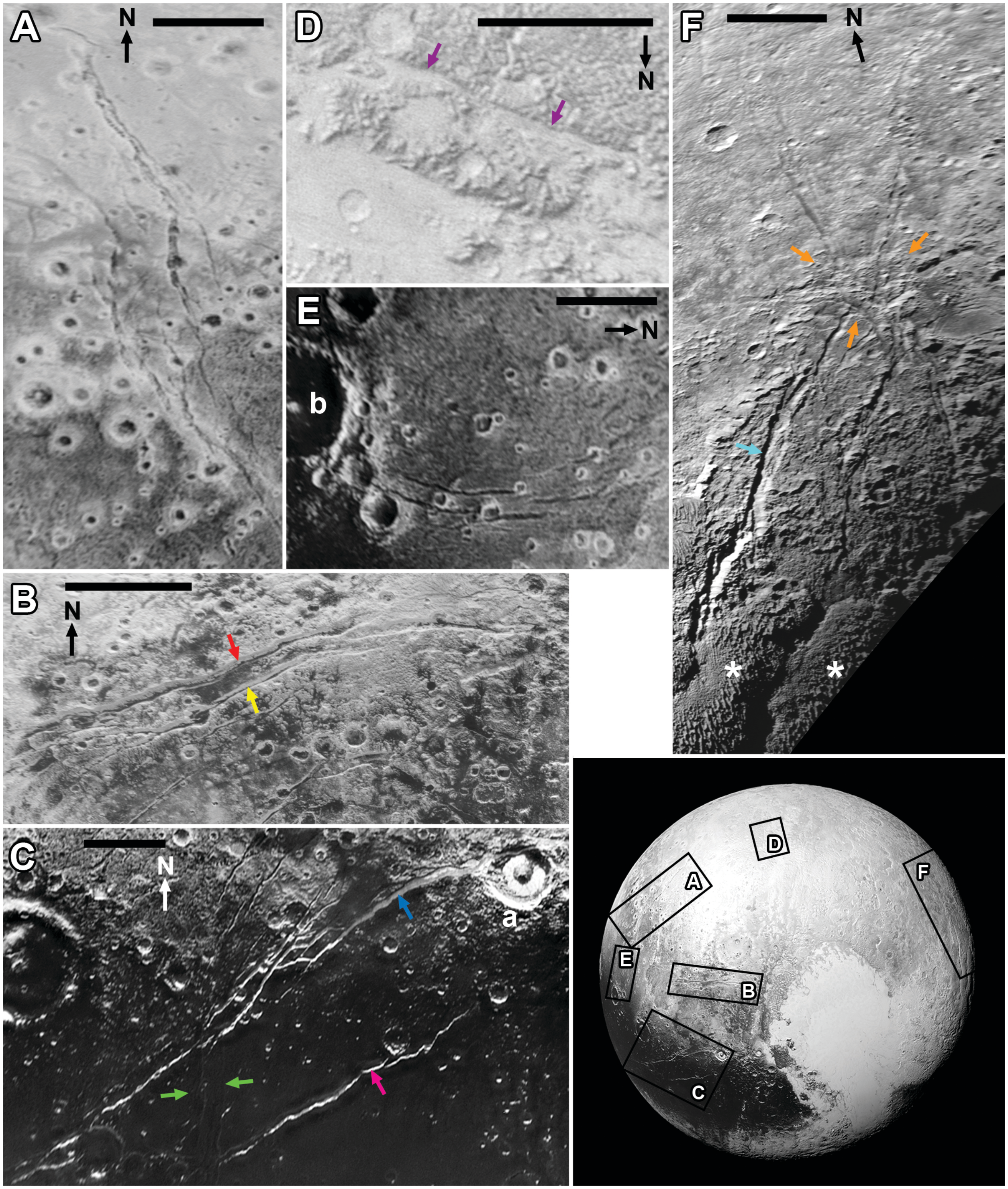

Fig. S9: **Tectonic features on Pluto.** Locations of the features on are highlighted in the figure at bottom-right. A and C-E are taken from 890 m/pixel, reprojected LORRI coverage from the P_LORRI observation, B is taken from 320 m/pixel, reprojected MVIC coverage of the

P_MVIC_LORRI_CA observation, and F is taken from 680 m/pixel MVIC coverage of the P_COLOR2 observation. Scale bars all measure 100 km. (A) Djanggawul Fossae; image centered at 41.1°N, 83.8°E. (B) Inanna (red arrow) and Dumuzi (yellow arrow) Fossae; image centered at 30.9°N, 131.5°E. (C) Virgil (blue arrow) and Beatrice (pink arrow) Fossae and Elliot crater (a), with the green arrows indicating a poorly illuminated south-trending set of fractures; image centered at 6.8°N, 126.1°E. (D) A heavily degraded graben in the northern uplands (purple arrows); image centered at 81.2°N, 99.1°E. (E) Djanggawul Fossae, emanating from Oort crater (b); image centered at 16.8°N, 92.3°E. (F) A set of fractures radiating from a central focus (orange arrows) to the north of Tartarus Dorsa (asterisks) and Sleipnir Fossa (cyan arrow); image centered at 31.8°N, 243.5°E.

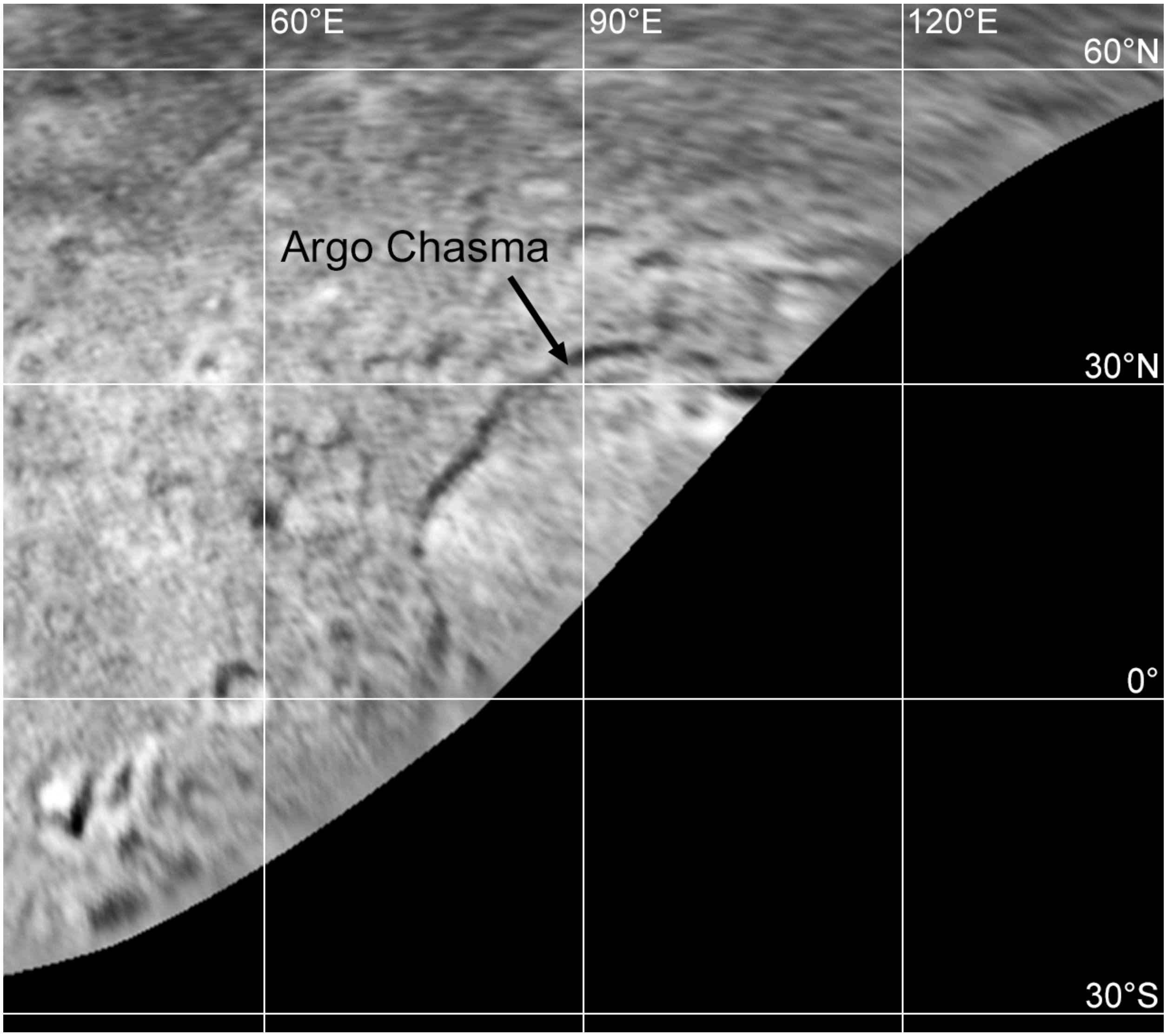

Fig. S10: **Argo Chasma in plan view.** Simple cylindrical projection of a portion of 5.32 km/pixel LORRI coverage from the PCNH_MULTI_LONG_1d1_01 observation. Projection covers Charon longitudes from 0° to 180°. Argo Chasma, seen obliquely during the encounter (Fig. S3 in (*5*)), is resolved in plan to be arcuate over at least 180°, and with a radius of ~175 km. Argo could thus be the rim of a (relaxed) impact basin, or alternatively, be tectonic in origin, and possibly related to the encounter hemisphere chasmata.

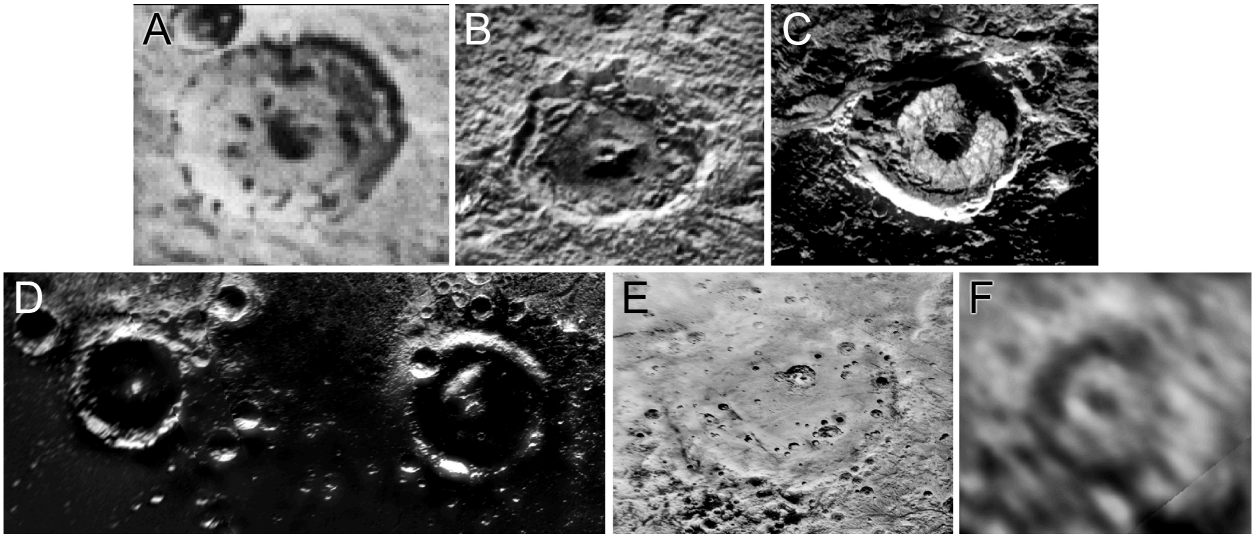

Fig. S11: **A variety of crater morphologies and albedos seen across Pluto.** (a) is 125 m/pixel LORRI coverage from the P_MPAN_1 observation; (b) to (e) is 320 m/pixel, reprojected MVIC coverage from the P_MVIC_LORRI_CA observation; (f) is 12.5 km/pixel LORRI coverage from the NAV_C4_L1_CRIT_37_01 observation. North is up in all cases. (a) 17 km diameter crater at 39°N, 139.5°E; (b) 45 km diameter Giclas crater at 39.5°N, 201.5°E; (c) 88 km diameter Elliot crater at 12°N, 138.5°E; (d) 120 km diameter Oort crater at 7.5°N, 91.5°E (left), and 140 km diameter Edgeworth crater at 6.5°N, 108.5°E; (e) 250 km diameter Burney crater at 45°N, 134.5°E; (f) 250 km diameter Simonelli crater at 13°N, 313.5°E.

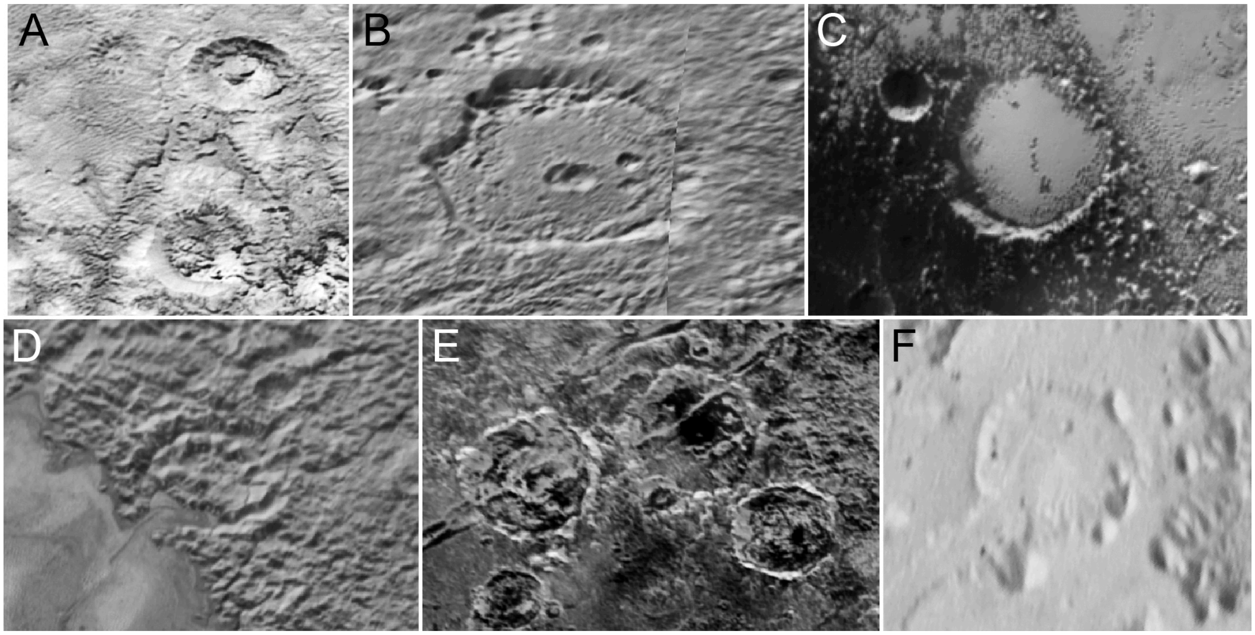

Fig. S12: **A variety of forms of crater degradation seen across Pluto.** (a) is from 390 m/pixel, reprojected LORRI coverage from the P_LORRI_STEREO_MOSAIC observation; (b) through (f) are from 320 m/pixel, reprojected MVIC coverage from the P_MVIC_LORRI_CA observation. (a) Craters displaying fluted walls. The two larger craters are each ~35 km across. Image centered at 46.5°N, 151°E. (b) 60 km diameter Kowal crater at 49°N, 217.5°E in the eroded mantle terrain. (c) 32.5 km diameter crater on the margin of Sputnik Planum at 4°S, 167°E, with ice covering its floor. (d) 36 km diameter Coradini crater on the margin of Sputnik Planum at 42.5°N, 191.5°E, which appears to have been dissected by steep, branched valley networks. (e) Craters cut by extensional fracturing in Viking Terra west of Sputnik Planum. The two larger craters are each ~45 km across. Image centered at 21.5°N, 130°E. (f) 37 km diameter crater at 78°N, 136°E, with a degraded rim and which appears to have been mantled by a bright deposit.

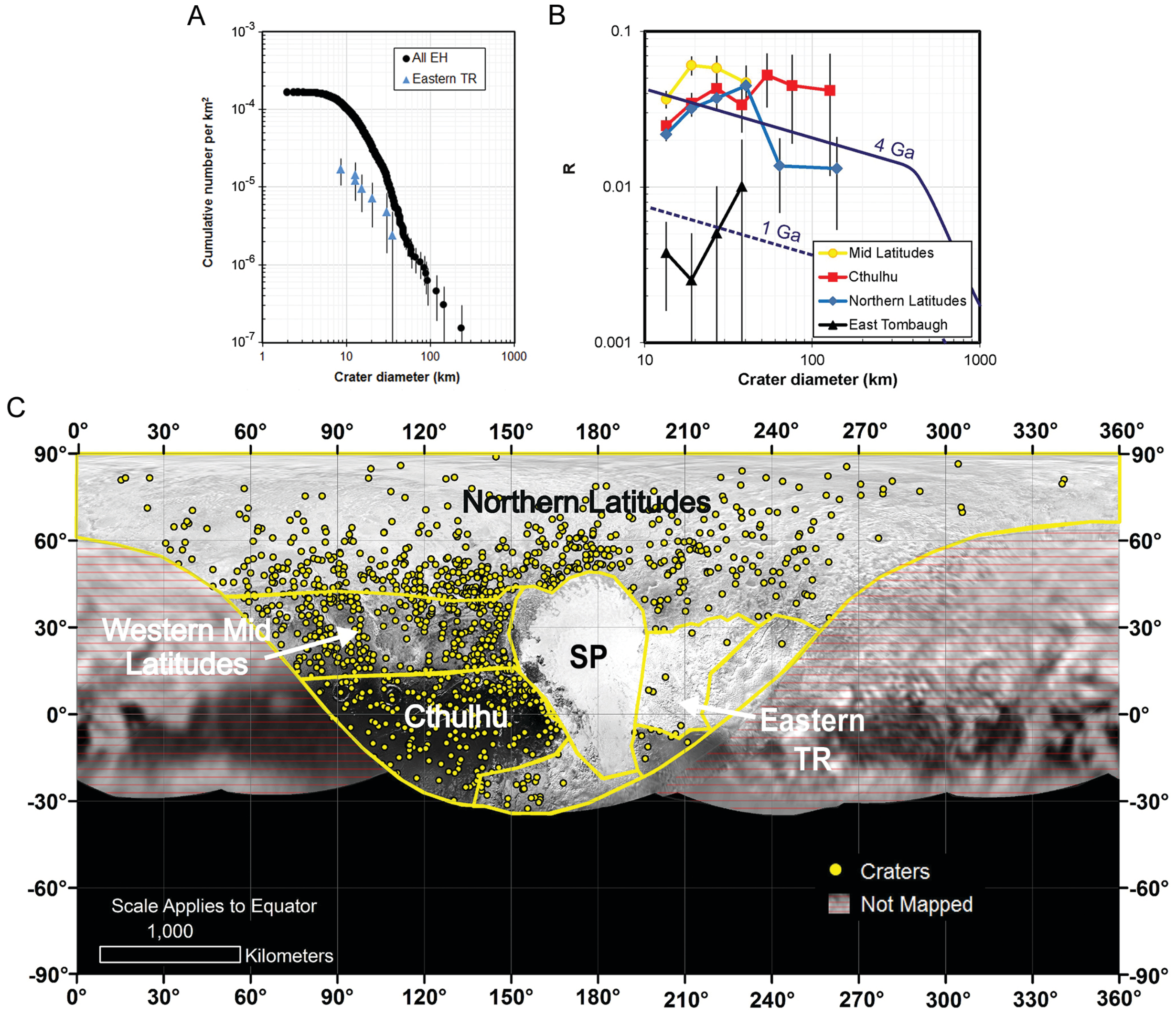

Fig. S13: **Crater statistics for Pluto.** (A) Cumulative size-frequency distribution for all craters in Pluto's encounter hemisphere, and those just within eastern Tombaugh Regio (TR), showing higher crater densities and an older age for Pluto as a whole compared with eastern Tombaugh Regio. (B) R-plot for craters within specific terrains in Pluto's encounter hemisphere. R-plots (or 'Relative' plots) plot differential crater counts relative to (divided by) a -3 power law distribution ($dN = kD^{-3}$), and highlight differences between different diameter ranges and surface units (*80*). The 4 Ga and 1 Ga age lines are predictions for expected crater densities for a given surface age for the broken power-law, or "knee", impactor distribution in (*11*), for reference; other impactor distributions in (*11*) give higher or lower R values for the same model age. (C) Map of the locations of all craters counted in Pluto's encounter hemisphere. Craters were mapped using 890 m/pixel LORRI coverage from the P_LORRI observation. Poisson ($\sqrt{N}$) errors are assumed in A and B.

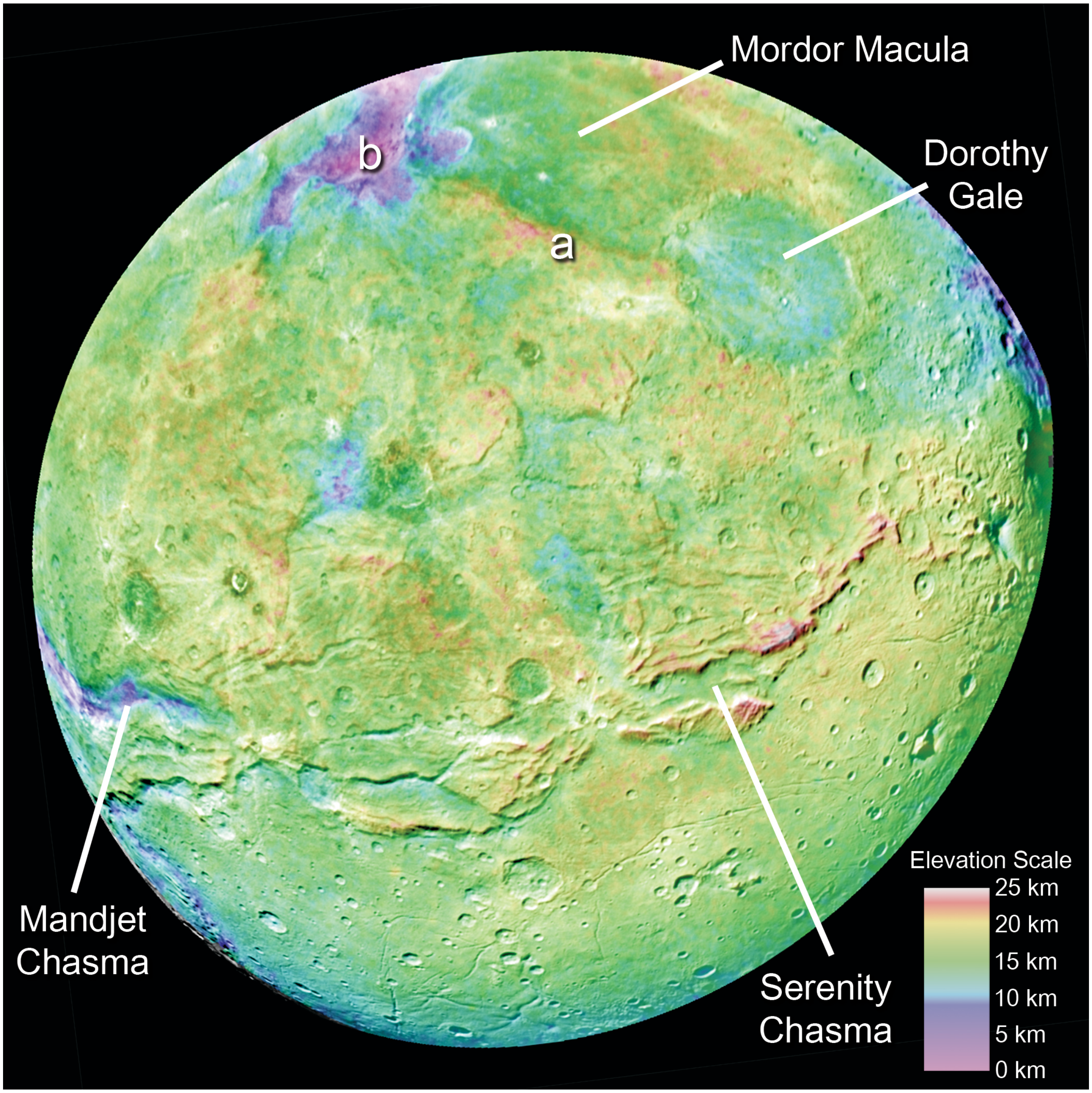

Fig. S14: **Colorized DEM of Charon's encounter hemisphere**. DEM is overlain on 1460 m/pixel MVIC coverage of the C_COLOR_2 observation. North is up. A prominent ridge (a) and an irregular depression (b) in the north polar region are highlighted.

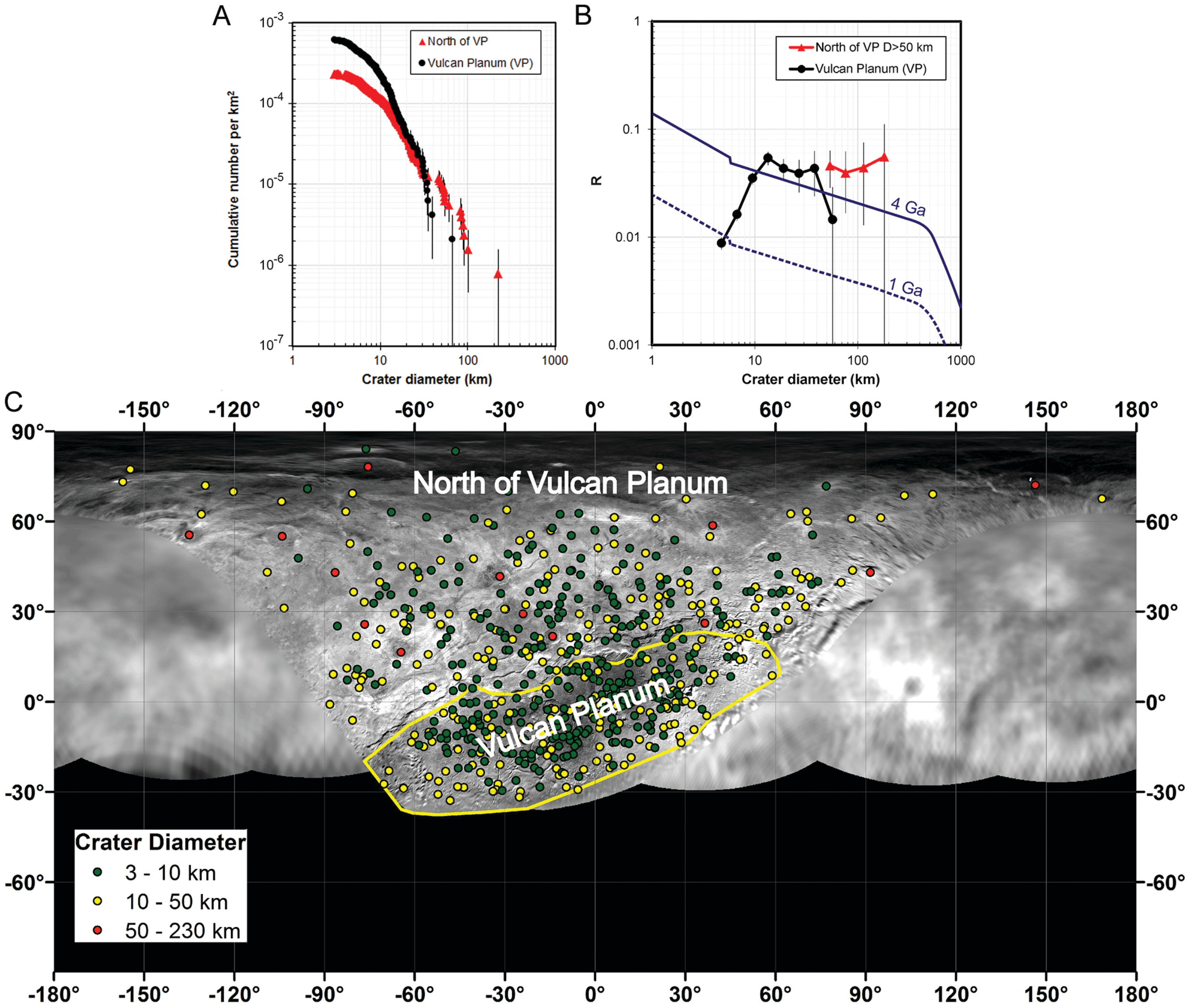

Fig. S15: **Crater statistics for Charon.** (A) Cumulative size-frequency distributions for craters within Vulcan Planum (VP) and craters north of Vulcan Planum on Charon. (B) R-plot for craters within Vulcan Planum and craters north of Vulcan Planum. (C) Map of the locations of all craters counted in Charon's encounter hemisphere. Craters were mapped using 890 m/pixel LORRI coverage from the C_LORRI observation. Poisson ($\sqrt{N}$) errors are assumed in A and B.

Table S1. **Possible convective properties of a 4-km deep N_2 ice layer on Pluto.**

$\delta T/h/\Delta T$	**3 K/100 m/20 K**	**3 K/1 km/20 K**	**3 K/100 m/9 K**	**6 K/100 m/9 K**
$\Delta\eta$	800	800	20	4.5
σ **(Pa)**	40	400	40	75
T_b **(K)**	56	56	45	45
η_b **(Pa-s)**	4.5×10^{12}	2.5×10^{11}	2.5×10^{13}	1×10^{13}
Ra_b	2.5×10^{6}	5×10^{7}	2×10^{5}	5×10^{5}
Nu	7	18	8	16
q **(mW/m^2)**	7	18	3.5	7.5

Temperature contrast (δT) and corresponding length (h) scale within the convective flow determines differential stress level (σ), which in turn determines basal viscosity (η_b) and Rayleigh number (Ra_b), and viscosity ratio $\Delta\eta = exp(\Delta T/\delta T)$ across the layer for a chosen basal temperature (T_b) and total temperature difference ΔT (from top to bottom). Different example combinations of δT, h, and ΔT are shown. Dimensionless and dimensional heat flows (Nu and q) are then estimated from scaling (*48*).

References and Notes

1. H. A. Weaver, W. C. Gibson, M. B. Tapley, L. A. Young, S. A. Stern, Overview of the New Horizons science payload. *Space Sci. Rev.* **140**, 75–91 (2008). doi:10.1007/s11214-008-9376-6

2. L. A. Young, S. A. Stern, H. A. Weaver, F. Bagenal, R. P. Binzel, B. Buratti, A. F. Cheng, D. Cruikshank, G. R. Gladstone, W. M. Grundy, D. P. Hinson, M. Horanyi, D. E. Jennings, I. R. Linscott, D. J. McComas, W. B. McKinnon, R. McNutt, J. M. Moore, S. Murchie, C. B. Olkin, C. C. Porco, H. Reitsema, D. C. Reuter, J. R. Spencer, D. C. Slater, D. Strobel, M. E. Summers, G. L. Tyler, New Horizons: Anticipated scientific investigations at the Pluto system. *Space Sci. Rev.* **140**, 93–127 (2008). doi:10.1007/s11214-008-9462-9

3. J. M. Moore, A. D. Howard, P. M. Schenk, W. B. McKinnon, R. T. Pappalardo, R. C. Ewing, E. B. Bierhaus, V. J. Bray, J. R. Spencer, R. P. Binzel, B. Buratti, W. M. Grundy, C. B. Olkin, H. J. Reitsema, D. C. Reuter, S. A. Stern, H. Weaver, L. A. Young, R. A. Beyer, Geology before Pluto: Pre-encounter considerations. *Icarus* **246**, 65–81 (2015). doi:10.1016/j.icarus.2014.04.028

4. Materials and methods are available as supplementary materials on *Science* Online.

5. S. A. Stern, F. Bagenal, K. Ennico, G. R. Gladstone, W. M. Grundy, W. B. McKinnon, J. M. Moore, C. B. Olkin, J. R. Spencer, H. A. Weaver, L. A. Young, T. Andert, J. Andrews, M. Banks, B. Bauer, J. Bauman, O. S. Barnouin, P. Bedini, K. Beisser, R. A. Beyer, S. Bhaskaran, R. P. Binzel, E. Birath, M. Bird, D. J. Bogan, A. Bowman, V. J. Bray, M. Brozovic, C. Bryan, M. R. Buckley, M. W. Buie, B. J. Buratti, S. S. Bushman, A. Calloway, B. Carcich, A. F. Cheng, S. Conard, C. A. Conrad, J. C. Cook, D. P. Cruikshank, O. S. Custodio, C. M. Dalle Ore, C. Deboy, Z. J. Dischner, P. Dumont, A. M. Earle, H. A. Elliott, J. Ercol, C. M. Ernst, T. Finley, S. H. Flanigan, G. Fountain, M. J. Freeze, T. Greathouse, J. L. Green, Y. Guo, M. Hahn, D. P. Hamilton, S. A. Hamilton, J. Hanley, A. Harch, H. M. Hart, C. B. Hersman, A. Hill, M. E. Hill, D. P. Hinson, M. E. Holdridge, M. Horanyi, A. D. Howard, C. J. Howett, C. Jackman, R. A. Jacobson, D. E. Jennings, J. A. Kammer, H. K. Kang, D. E. Kaufmann, P. Kollmann, S. M. Krimigis, D. Kusnierkiewicz, T. R. Lauer, J. E. Lee, K. L. Lindstrom, I. R. Linscott, C. M. Lisse, A. W. Lunsford, V. A. Mallder, N. Martin, D. J. McComas, R. L. McNutt Jr., D. Mehoke, T. Mehoke, E. D. Melin, M. Mutchler, D. Nelson, F. Nimmo, J. I. Nunez, A. Ocampo, W. M. Owen, M. Paetzold, B. Page, A. H. Parker, J. W. Parker, F. Pelletier, J. Peterson, N. Pinkine, M. Piquette, S. B. Porter, S. Protopapa, J. Redfern, H. J. Reitsema, D. C. Reuter, J. H. Roberts, S. J. Robbins, G. Rogers, D. Rose, K. Runyon, K. D. Retherford, M. G. Ryschkewitsch, P. Schenk, E. Schindhelm, B. Sepan, M. R. Showalter, K. N. Singer, M. Soluri, D. Stanbridge, A. J. Steffl, D. F. Strobel, T. Stryk, M. E. Summers, J. R. Szalay, M. Tapley, A. Taylor, H. Taylor, H. B. Throop, C. C. Tsang, G. L. Tyler, O. M. Umurhan, A. J. Verbiscer, M. H. Versteeg, M. Vincent, R. Webbert, S. Weidner, G. E. Weigle 2nd, O. L. White, K. Whittenburg, B. G. Williams, K. Williams, S. Williams, W. W. Woods, A. M. Zangari, E. Zirnstein, The Pluto system: Initial results from its exploration by New Horizons. *Science* **350**, aad1815 (2015). Medline

6. J. Eluszkiewicz, D. J. Stevenson, Rheology of solid methane and nitrogen: Applications to Triton. *Geophys. Res. Lett.* **17**, 1753–1756 (1990). doi:10.1029/GL017i010p01753

7. Y. Yamashita, M. Kato, M. Arakawa, Experimental study on the rheological properties of polycrystalline solid nitrogen and methane: Implications for tectonic processes on Triton. *Icarus* **207**, 972–977 (2010). doi:10.1016/j.icarus.2009.11.032

8. W. M. Grundy, R. P. Binzel, B. J. Buratti, J. C. Cook, D. P. Cruikshank, C. M. Dalle Ore, A. M. Earle, K. Ennico, C. J. A. Howett, A. W. Lunsford, C. B. Olkin, A. H. Parker, S. Philippe, S. Protopapa, E. Quirico, D. C. Reuter, B. Schmitt, K. N. Singer, A. J. Verbiscer, R. A. Beyer, M. W. Buie, A. F. Cheng, D. E. Jennings, I. R. Linscott, J. W. Parker, P. M. Schenk, J. R. Spencer, J. A. Stansberry, S. A. Stern, H. B. Throop, C. C. C. Tsang, H. A. Weaver, G. E. Weigle II, L. A. Young, New Horizons Science Team, Surface compositions across Pluto and Charon. *Science* **351**, aad9189 (2016).

9. G. C. Collins, W. B. McKinnon, J. M. Moore, F. Nimmo, R. T. Pappalardo, L. M. Prockter, P. M. Schenk, Tectonics of the outer planet satellites, in *Planetary Tectonics*, R. A. Schultz, T. R. Watters, Eds. (Cambridge Univ. Press, NY, 2010), pp. 264–350.

10. R. Gomes, H. F. Levison, K. Tsiganis, A. Morbidelli, Origin of the cataclysmic Late Heavy Bombardment period of the terrestrial planets. *Nature* **435**, 466–469 (2005). Medline doi:10.1038/nature03676

11. S. Greenstreet, B. Gladman, W. B. McKinnon, Impact and cratering rates onto Pluto. *Icarus* **258**, 267–288 (2015). doi:10.1016/j.icarus.2015.05.026

12. G. R. Gladstone, S. A. Stern, K. Ennico, C. B. Olkin, H. A. Weaver, L. A. Young, M. E. Summers, D. F. Strobel, D. P. Hinson, J. A. Kammer, A. H. Parker, A. J. Steffl, I. R. Linscott, J. W. Parker, A. F. Cheng, D. C. Slater, M. H. Versteeg, T. K. Greathouse, K. D. Retherford, H. Throop, N. J. Cunningham, W. W. Woods, K. N. Singer, C. C. C. Tsang, E. Schindhelm, C. M. Lisse, M. L. Wong, Y. L. Yung, X. Zhu, W. Curdt, P. Lavvas, E. F. Young, G. L. Tyler, New Horizons Science Team, The atmosphere of Pluto as observed by New Horizons. *Science* **351**, aad8866 (2016).

13. K. N. Singer, S. A. Stern, On the provenance of Pluto's nitrogen (N_2). *Astrophys. J.* **808**, L50 (2015). doi:10.1088/2041-8205/808/2/L50

14. G. Robuchon, F. Nimmo, Thermal evolution of Pluto and implications for surface tectonics and a subsurface ocean. *Icarus* **216**, 426–439 (2011). doi:10.1016/j.icarus.2011.08.015

15. M. Brozović, M. R. Showalter, R. A. Jacobson, M. W. Buie, The orbits and masses of satellites of Pluto. *Icarus* **246**, 317–329 (2015). doi:10.1016/j.icarus.2014.03.015

16. P. M. Schenk, J. M. Moore, Geologic landforms and processes on icy satellites, in *Solar System Ices*, B. Schmitt, C. de Bergh, M. Festou, Eds. (Kluwer Academic, Dordrecht, 1998), pp. 551–578.

17. D. G. Jankowski, S. W. Squyres, Solid-state ice volcanism on the satellites of Uranus. *Science* **241**, 1322–1325 (1988). Medline doi:10.1126/science.241.4871.1322

18. L. M. Prockter, R. M. C. Lopes, B. Giese, R. Jaumann, R. D. Lorenz, R. T. Pappalardo, G. W. Patterson, P. C. Thomas, E. P. Turtle, R. J. Wagner, Characteristics of icy surfaces. *Space Sci. Rev.* **153**, 63–111 (2010). doi:10.1007/s11214-010-9649-8

19. G. Schubert, H. Hussmann, V. Lainey, D. L. Matson, W. B. McKinnon, F. Sohl, C. Sotin, G. Tobie, D. Turrini, T. Van Hoolst, Evolution of icy satellites. *Space Sci. Rev.* **153**, 447–484 (2010). doi:10.1007/s11214-010-9635-1

20. M. Manga, C.-Y. Wang, Pressurized oceans and the eruption of liquid water on Europa and Enceladus. *Geophys. Res. Lett.* **34**, L07202 (2007). doi:10.1029/2007GL029297

21. E. L. Schaller, M. E. Brown, Volatile loss and retention on Kuiper Belt objects. *Astrophys. J.* **659**, L61–L64 (2007). doi:10.1086/516709

22. W. B. McKinnon, Introduction to 'Pluto, Charon, and the Kuiper Belt Objects': Pluto on the eve of the New Horizons Encounter, in *Treatise on Geophysics,* G. Schubert, Ed. (Elsevier, Amsterdam, ed. 2, 2015), vol. 10, pp. 637–651. doi:10.1016/B978-0-444-53802-4.00210-4

23. D. C. Reuter, S. A. Stern, J. Scherrer, D. E. Jennings, J. W. Baer, J. Hanley, L. Hardaway, A. Lunsford, S. McMuldroch, J. Moore, C. Olkin, R. Parizek, H. Reitsma, D. Sabatke, J. Spencer, J. Stone, H. Throop, J. Van Cleve, G. E. Weigle, L. A. Young, Ralph: A visible/infrared imager for the New Horizons Pluto/Kuiper Belt mission. *Space Sci. Rev.* **140**, 129–154 (2008). doi:10.1007/s11214-008-9375-7

24. P. M. Schenk, A. McEwen, A. G. Davies, T. Davenport, K. Jones, B. Fessler, Geology and topography of Ra Patera, Io, in the Voyager era: Prelude to eruption. *Geophys. Res. Lett.* **24**, 2467–2470 (1997). doi:10.1029/97GL02688

25. P. M. Schenk, M. H. Bulmer, Origin of mountains on Io by thrust faulting and large-scale mass movements. *Science* **279**, 1514–1517 (1998). Medline doi:10.1126/science.279.5356.1514

26. P. M. Schenk, Thickness constraints on the icy shells of the Galilean satellites from a comparison of crater shapes. *Nature* **417**, 419–421 (2002). Medline doi:10.1038/417419a

27. P. M. Schenk, R. R. Wilson, A. G. Davies, Shield volcano topography and the rheology of lava flows on Io. *Icarus* **169**, 98–110 (2004). doi:10.1016/j.icarus.2004.01.015

28. O. L. White, P. M. Schenk, A. J. Dombard, Impact basin relaxation on Rhea and Iapetus and relation to past heat flow. *Icarus* **223**, 699–709 (2013). doi:10.1016/j.icarus.2013.01.013

29. O. L. White, P. M. Schenk, F. Nimmo, T. Hoogenboom, A new stereo topographic map of Io: Implications for geology from global to local scales. *J. Geophys. Res. Planets* **119**, 1276–1301 (2014). doi:10.1002/2013JE004591

30. S. A. Stern, The Pluto-Charon Systems. *Annu. Rev. Astron. Astrophys.* **30**, 185–233 (1992). doi:10.1146/annurev.aa.30.090192.001153

31. S. Byrne, A. P. Ingersoll, A sublimation model for martian south polar ice features. *Science* **299**, 1051–1053 (2003). Medline doi:10.1126/science.1080148

32. V. F. Petrenko, R. W. Whitworth, *Physics of Ice* (Oxford Univ. Press, Oxford, 1999).

33. J. Besserer, F. Nimmo, J. H. Roberts, R. T. Pappalardo, Convection-driven compaction as a possible origin of Enceladus's long wavelength topography. *J. Geophys. Res. Planets* **118**, 908–915 (2013). doi:10.1002/jgre.20079

34. M. A. Wieczorek, G. A. Neumann, F. Nimmo, W. S. Kiefer, G. J. Taylor, H. J. Melosh, R. J. Phillips, S. C. Solomon, J. C. Andrews-Hanna, S. W. Asmar, A. S. Konopliv, F. G. Lemoine, D. E. Smith, M. M. Watkins, J. G. Williams, M. T. Zuber, The crust of the Moon as seen by GRAIL. *Science* **339**, 671–675 (2013). Medline doi:10.1126/science.1231530

35. G. Collins, F. Nimmo, Chaotic Terrain on Europa, in *Europa*, R. T. Pappalardo, W. B. McKinnon, K. K. Khurana, Eds. (Univ. of Arizona Press, Tucson, AZ, 2009), pp. 259–281.

36. P. M. Schenk, F. Nimmo, W. B. McKinnon, J. M. Moore, K. Ennico, S. A . Stern, C. Olkin, L.A. Young, H. Weaver, and the New Horizons Science Team, A large impact origin for Sputnik Planum and surrounding terrains, Pluto? *AAS DPS 47th Annual Meeting*, abstract 200.06 (2015).

37. T. A. Scott, Solid and liquid nitrogen. *Phys. Rep.* **27**, 89–157 (1976). doi:10.1016/0370-1573(76)90032-6

38. R. H. Brown, R. L. Kirk, Coupling of volatile transport and internal heat flow on Triton. *J. Geophys. Res.* **99**, 1965–1981 (1994). doi:10.1029/93JE02618

39. E. Fukushima, A. A. V. Gibson, T. A. Scott, Pressure dependence of the melting and α-β phase transition temperatures of carbon monoxide. *J. Low Temp. Phys.* **28**, 157–165 (1977). doi:10.1007/BF00658965

40. R. B. Yelle, J. I. Lunine, J. B. Pollack, R. H. Brown, Lower atmospheric structure and surface-atmosphere interactions on Triton, in *Neptune and Triton*, D. P. Cruikshank, A. Morbidelli, Eds. (Univ. of Arizona Press, Tucson, AZ, 1995), pp. 1031–1106.

41. W. S. B. Paterson, *The Physics of Glaciers* (Oxford Univ. Press, Oxford, ed. 3, 2001).

42. W. B. McKinnon, Convective instability in Europa's floating ice shell. *Geophys. Res. Lett.* **26**, 951–954 (1999). doi:10.1029/1999GL900125

43. V. S. Solomatov, Scaling of temperature- and stress-dependent viscosity convection. *Phys. Fluids* **7**, 266–274 (1995). doi:10.1063/1.868624

44. L. N. Moresi, V. S. Solomatov, Numerical investigation of 2D convection with extremely large viscosity variations. *Phys. Fluids* **7**, 2154–2162 (1995). doi:10.1063/1.868465

45. J. A. Stansberry, R. V. Yelle, Emissivity and the fate of Pluto's atmosphere. *Icarus* **141**, 299–306 (1999). doi:10.1006/icar.1999.6169

46. N. P. Hammond, A. C. Barr, Formation of Ganymede's grooved terrain by convection-driven resurfacing. *Icarus* **227**, 206–209 (2014). doi:10.1016/j.icarus.2013.08.024

47. V. S. Solomatov, L.-N. Moresi, Scaling of time-dependent stagnant lid convection: Application to small-scale convection on Earth and other terrestrial planets. *J. Geophys. Res.* **105**, 21,795–21,817 (2000). doi:10.1029/2000JB900197

48. A. C. Barr, Mobile lid convection beneath Enceladus' south polar terrain. *J. Geophys. Res. Planets* **113**, E07009 (2008). doi:10.1029/2008JE003114

49. W. B. McKinnon, D. P. Simonelli, G. Schubert, Composition, internal structure, and thermal evolution of Pluto and Charon, in *Pluto and Charon*, S. A. Stern, D. J. Tholen, Eds. (Univ. of Arizona Press, Tucson, AZ, 1997), pp. 295–343.

50. W. B. McKinnon, On convection in ice I shells of outer Solar System bodies, with detailed application to Callisto. *Icarus* **183**, 435–450 (2006). doi:10.1016/j.icarus.2006.03.004

51. W. B. Durham, O. Prieto-Ballesteros, D. L. Goldsby, J. S. Kargel, Rheological and thermal properties of icy materials. *Space Sci. Rev.* **153**, 273–298 (2010). doi:10.1007/s11214-009-9619-1

52. V. S. Solomatov, L.-N. Moresi, Three regimes of mantle convection with non-Newtonian viscosity and stagnant lid convection on the terrestrial planets. *Geophys. Res. Lett.* **24**, 1907–1910 (1997). doi:10.1029/97GL01682

53. D. L. Goldsby, D. L. Kohlstedt, Superplastic deformation of ice: Experimental observations. *J. Geophys. Res. Solid Earth* **106**, 11017–11030 (2001). doi:10.1029/2000JB900336

54. J. W. Glen, The creep of polycrystalline ice. *Proc. R. Soc. London Ser. A* **228**, 519–538 (1955). doi:10.1098/rspa.1955.0066

55. D. Benn, D. J. A. Evans, *Glaciers and Glaciation* (Hodder Education, 2010).

56. M. D. Betterton, Theory of structure formation in snowfields motivated by penitentes, suncups, and dirt cones. *Phys. Rev. E Stat. Nonlin. Soft Matter Phys.* **63**, 056129 (2001). Medline doi:10.1103/PhysRevE.63.056129

57. L. Lliboutry, The origin of penitents. *J. Glaciol.* **2**, 331–338 (1954).

58. V. Bergeron, C. Berger, M. D. Betterton, Controlled irradiative formation of penitentes. *Phys. Rev. Lett.* **96**, 098502 (2006). Medline doi:10.1103/PhysRevLett.96.098502

59. T. Tiedje, K. A. Mitchell, B. Lau, A. Ballestad, E. Nodwell, Radiation transport model for ablation hollows on snowfields. *J. Geophys. Res.* **111**, F02015 (2006). doi:10.1029/2005JF000395

60. J. J. Rhodes, R. L. Armstrong, S. G. Warren, Mode of formation of "ablation hollows" controlled by dirt content of snow. *J. Glaciol.* **33**, 135–139 (1987).

61. A. D. Howard, Origin of the stepped topography of the martian poles. *Icarus* **34**, 581–599 (1978). doi:10.1016/0019-1035(78)90047-7

62. I. B. Smith, J. W. Holt, Onset and migration of spiral troughs on Mars revealed by orbital radar. *Nature* **465**, 450–453 (2010). Medline doi:10.1038/nature09049

63. M. D. Cline, N. R. Iverson, C. Harding, Origin of washboard moraines of the Des Moines Lobe: Spatial analyses with LiDAR data. *Geomorphology* **246**, 570–578 (2015). doi:10.1016/j.geomorph.2015.07.021

64. D. K. Kieffer, A. M. Johnson, Earth flows: Morphology, mobilization, and movement. U. S. Geological Survey Prof. Paper 1264 (1983).

65. F. E. Matthes, Avalanche sculpture in the Sierra Nevada of California. *Int. Assoc. Sci. Hydrol. Bull.* **23**, 631–637 (1938).

66. B. H. Luckman, The geomorphic activity of snow avalanches. *Geogr. Ann., Ser. A* **59**, 31–48 (1977). doi:10.2307/520580

67. C. M. Dundas, S. Diniega, C. J. Hansen, S. Byrne, A. S. McEwen, Seasonal activity and morphological changes in martian gullies. *Icarus* **220**, 124–143 (2012). doi:10.1016/j.icarus.2012.04.005

68. K. R. MacGregor, R. S. Anderson, E. D. Waddington, Numerical modeling of glacial erosion and headwall processes in alpine valleys. *Geomorphology* **103**, 189–204 (2009). doi:10.1016/j.geomorph.2008.04.022

69. R. S. Anderson, P. Molnar, M. A. Kessler, Features of glacial valley profiles simply explained. *J. Geophys. Res.* **111**, F01004 (2006). doi:10.1029/2005JF000344

70. M. A. Kessler, R. S. Anderson, J. P. Briner, Fjord insertion into continental margins driven by topographic steering of ice. *Nat. Geosci.* **1**, 365–369 (2008). doi:10.1038/ngeo201

71. A. D. Howard, A detachment-limited model of drainage basin evolution. *Water Resour. Res.* **30**, 2261–2285 (1994). doi:10.1029/94WR00757

72. P. Sternai, F. Herman, J.-D. Champagnac, M. Fox, B. Salcher, S. D. Willett, Pre-glacial topography of the European Alps. *Geology* **40**, 1067–1070 (2012). doi:10.1130/G33540.1

73. R. S. Anderson, Evolution of lumpy glacial landscapes. *Geology* **42**, 679–682 (2014). doi:10.1130/G35537.1

74. F. Herman, F. Beaud, J.-D. Champagnac, J.-M. Lemieux, P. Sternai, Glacial hydrology and erosion patterns: A mechanism for carving glacial valleys. *Earth Planet. Sci. Lett.* **310**, 498–508 (2011). doi:10.1016/j.epsl.2011.08.022

75. E. F. Gjermundsen, J. P. Briner, N. Akçar, J. Foros, P. W. Kubik, O. Salvigsen, A. Hormes, Minimal erosion of Arctic alpine topography during late Quaternary glaciation. *Nat. Geosci.* **8**, 789–792 (2015). doi:10.1038/ngeo2524

76. J. W. Head, D. R. Marchant, Cold-based mountain glaciers on Mars: Western Arsia Mons. *Geology* **31**, 641–644 (2003). doi:10.1130/0091-7613(2003)031<0641:CMGOMW>2.0.CO;2

77. C. B. Atkins, P. J. Barrett, S. R. Hicock, Cold glaciers erode and deposit: Evidence from Allan Hills, Antarctica. *Geology* **30**, 659–662 (2002). doi:10.1130/0091-7613(2002)030<0659:CGEADE>2.0.CO;2

78. M. J. Hambrey, S. J. Fitzsimons, Development of sediment-landform associations at cold glacier margins, Dry Valleys, Antarctica. *Sedimentology* **57**, 857–882 (2010). doi:10.1111/j.1365-3091.2009.01123.x

79. A. S. Krassilnikov, J. W. Head, Novae on Venus: Geology, classification, and evolution. *J. Geophys. Res. Planets* **108**, 5108 (2003). doi:10.1029/2002JE001983

80. Crater Analysis Techniques Working Group, Standard techniques for presentation and analysis of crater size-frequency data. *Icarus* **37**, 467–474 (1979). doi:10.1016/0019-1035(79)90009-5

81. E. B. Bierhaus, L. Dones, Craters and ejecta on Pluto and Charon: Anticipated results from the New Horizons flyby. *Icarus* **246**, 165–182 (2015). doi:10.1016/j.icarus.2014.05.044

82. K. N. Singer, W. B. McKinnon, S. J. Robbins, P. M. Schenk, S. Greenstreet, B. Gladman, A. H. Parker, S. A. Stern, V. J. Bray, H. A. Weaver, R. A. Beyer, L. A. Young, J. R. Spencer, J. M. Moore, C. B. Olkin, K. Ennico, R. P. Binzel, W. M. Grundy, The New Horizons Geology, Geophysics and Imaging Science Theme Team, The New Horizons Surface Composition Science Theme Team, The New Horizons MVIC and LORRI Teams, Craters on Pluto and Charon—Surface ages and impactor populations. *47*th *Lunar Planet. Sci. Conf.*, abstract 2310 (2016).

83. S. Greenstreet, B. Gladman, W. B. McKinnon, Corrigendum to (*11*), submitted.